



## Supplementary Materials for

### **Substantial convection and precipitation enhancements by ultrafine aerosol particles**

Jiwen Fan,\* Daniel Rosenfeld, Yuwei Zhang, Scott E. Giangrande, Zhanqing Li, Luiz A. T. Machado, Scot T. Martin, Yan Yang, Jian Wang, Paulo Artaxo, Henrique M. J. Barbosa, Ramon C. Braga, Jennifer M. Comstock, Zhe Feng, Wenhua Gao, Helber B. Gomes, Fan Mei, Christopher Pöhlker, Mira L. Pöhlker, Ulrich Pöschl, Rodrigo A. F. de Souza

\*Corresponding author. Email: [jiwen.fan@pnnl.gov](mailto:jiwen.fan@pnnl.gov)

Published 26 January 2018, *Science* **359**, 411 (2018)  
DOI: 10.1126/science.aan8461

#### **This PDF file includes:**

Materials and Methods  
Supplementary Text  
Figs. S1 to S17  
Table S1  
References

## Materials and Methods

### Observational data analysis

To analyze the relationship between updraft velocity, radar reflectivity, and surface precipitation with aerosol concentrations ( $N_a$ ) as shown in Fig. 2, we only selected the locally occurring systems for the wet season of 2014 from 01 March to 31 May based on criteria in Tang et al. (33) to constrain the selected convective cases occurring within similar pre-storm environments. The selection criteria are (1) convection occurred between 11:00-19:00 local time and (2) no convection occurred during the 3 hours preceding the locally occurring systems. The second criterion excludes cases with previously existing convective clouds, which are likely from the propagating systems. We further applied another criterion to ensure deep convective clouds: the maximum echo height determined by reflectivity  $> 0$  dBZ measured by UHF (1290 MHz) Atmospheric Radiation Measurement (ARM) Radar Wind Profiler (RWP) for each event is higher than 10 km.

There were 20 cases meeting the above criteria during the analysis period. However, aerosol measurements from the Scanning-Mobility Particle Sizer (SMPS) for three of the events were reported as having bad data, which left 17 qualifying locally occurring cases: the 11, 17, 22, 23 and 26 events in March; the 1, 12, 18, 20, 21, 23 and 25 events in April; and the 16, 19, 20, 30, and 31 events in May (Table S1). The low-level air for these cases was generally northeasterly, favoring the transport of the Manaus pollution plume to the T3 site. The vertical velocity data were retrieved from the ARM RWP (31-32), and have a vertical resolution of 120 m and temporal resolution  $\sim 6$  s. The accuracy of the RWP retrievals is expected to be within 1 to 2  $\text{m s}^{-1}$  within convective updrafts that do not indicate large hail. The radar reflectivity measurements provide an estimate of the microphysical properties related to storm precipitation properties available from the RWP and have similar temporal and spatial resolutions as these vertical velocity retrievals.

Accurate surface rain rate (having the highest temporal resolution for deep convective cloud systems) is also retrieved from the RWP, merged with local rain gauge measurements. The environmental convective available potential energy (CAPE) and convective inhibition (CIN) values for each convective case are calculated from the nearest available radiosonde launch before the convective event. Because soundings are launched at a minimum of four times per day (up to six times per day in March that is during the Intensive Operation Period 1) at the T3 site, the CAPE and CIN calculated in this way should be representative for the respective convective event. There was no retrieval from the RWP between 3.5- and 5.5-km altitudes due to retrieval contamination from melting particles. We obtained aerosol size distribution data from the SMPS at 5-min intervals at the T3 site. The standard SMPS instrument measures the aerosol number size distribution in the particle diameter range from 10 to 500 nm. The uncertainty for the data at T3 is largely dominated by the variability in the sampling flow rate, which is around  $\pm 10\%$ . For each convective event, aerosols were averaged over the 30-min time period right before convective clouds occurred over the T3 site. The aerosol concentrations are shown in Table S1. All observational datasets from this study can be

obtained from the U.S. Department of Energy's ARM program data archive  
<http://www.archive.arm.gov/discovery/#v/results/s/fiop::amf2014goamazon>.

To help exclude other factors that might contribute to the positive correlation between updraft velocity and aerosols, in addition to CAPE and CIN, we examined changes in profiles of temperature (T), relative humidity (RH), zonal (U) and meridional (V) component winds from the lower to higher aerosol groups as shown in Fig. S3. From those plots, we can also know if there are significant contributions from boundary layer dynamics and middle-level moisture to deep cloud development. As shown in Fig. S3, none of these factors seem to explain an increasing relationship of updraft intensity with the increase of  $UAP_{<50}$ .

### Model experiments

We conducted model simulations for a locally occurring system occurring on 17 March 2014 using the Weather Research and Forecasting (WRF) model v3.6.1 (38) with the spectral-bin microphysics (SBM) (36-37). The local convective cells were observed at 1600-1900 UTC around the T3 site where the U.S. Department of Energy ARM Mobile Facility was located (Fig. S4A) during GoAmazon2014/5, by the X-band radar located at the T3 site and the S-band radar (SIPAM) located at the Manaus metropolis (near the T1 site), 67.8 km northeast of the T3 site. The radar reflectivity reached its largest values at 1800-1830 UTC (Fig. S4A). The low-level wind was northeasterly (Fig. S4B), favoring the transport of the Manaus pollution plume to the T3 site. The cloud bases were warm (about 20 °C) with weak wind shear in the lower troposphere. The estimated CAPE value was very high (around 4500 J kg<sup>-1</sup>) approximately 2 h before the initiation of convection.

We performed the simulations using realistic initial and lateral boundary conditions. The land surface data used for the simulations were the best available products for South America. The soil moisture was from an operational product from Center for Weather Forecasting and Climate Research/National Institute of Space Research (CPTEC/INPE) in Brazil, which is a daily product at 0.25 degree (49). The surface albedo, vegetation, and green fraction used in this study are documented in Beck et al. (50). Two nested domains with horizontal grids of 1 and 0.5 km are used (Fig. S5A) with 51 vertical levels up to 50 hPa. The numbers of horizontal grid points for Domain 1 and Domain 2 are 1000×1000 and 450×450, respectively. The Domain 1 simulation is driven by the National Center for Environmental Prediction final analysis data (NCEP/FNL) at 1-degree horizontal resolution and 6-h temporal intervals and run with the Morrison two-moment microphysics scheme (51-52). We ran Domain 1 over a large region (1000 km) with such a high resolution (1 km) to better simulate the mesoscale features over the Amazon Basin so that it could provide more accurate dynamics and thermodynamics to Domain 2 simulations. We purposely avoided using grey-zone resolutions (4-50 km in cumulus parameterization). To buffer the “jump” from the 1-degree NCEP/FNL data to 1-km horizontal grid spacing, we employed 30 grid points for each side of the lateral boundaries in Domain 1. We ran all of the simulations over Domain 2 with the SBM using the “ndown” approach. That is, these simulations were driven by the same initial and lateral boundary meteorological conditions derived from Domain 1 outputs with the lateral boundary conditions updated every 3 h. The SBM employed is the fast version,

which solves a system of kinetic equations for the size distribution functions of water drops, ice crystals/snow, graupel, as well as cloud condensation nuclei (CCN). The diffusional growth processes (i.e., condensation/evaporation and deposition/sublimation) in SBM are calculated with theoretical equations based on the predicted supersaturation and particle size. We used the Yonsei University planetary boundary layer scheme, Unified Noah land surface scheme, and the rapid radiative transfer model for general circulation model (RRTMG) longwave and shortwave radiation schemes in this study. Cumulus parameterization was not needed for the simulations in both domains. The modeled dynamic time step was 5 s for 1-km resolution and 3 s for 0.5-km resolution, and simulations were initiated at 12:00 UTC on 16 March, and run for 36 h. The simulation output frequency used for the analysis was 5-min.

Table 1 summarizes the major simulations for this study. C\_BG is the simulation with a present-day background  $N_a$  in the Manaus region of  $950 \text{ cm}^{-3}$  (130 for  $\text{CCN}_{>50}$  and 820 for  $\text{UAP}_{<50}$ ) near the surface. The plume affected case is P3\_BG, which is based on C\_BG, but  $N_a$  at the Manaus metropolis (black box in Fig. S5B) is increased by a factor of 3, and set as a constant plume source during the model simulation to mimic the observed Manaus pollution plume. Aerosol size distribution (SD) is shown in Fig. S5C. For  $\text{UAP}_{<50}$ , the power-law relationship followed the observed shape in the Manaus city (Line 1 in Fig. S6C). The total  $\text{UAP}_{<50}$  concentration of  $2460 \text{ cm}^{-3}$  in the P3\_BG yields cloud droplet concentrations of about  $300 \text{ cm}^{-3}$  in the warm-cloud period, which is within the range of  $200\text{-}600 \text{ cm}^{-3}$  for the plume-affected warm clouds observed for this case by aircraft. For  $\text{CCN}_{>50}$ , the SD was adapted from measurements under present-day pristine conditions approximating pre-industrial conditions at the remote rainforest site of the Amazonian Tall Tower Observatory (ATTO) in the central Amazon Basin (black line in Fig. 6a of ref. 39) and scaled to  $130 \text{ cm}^{-3}$  of  $\text{CCN}_{>50}$  (35<sup>th</sup> percentile) while keeping the shape similar to the SD averaged over all ATTO measurements under present-day pristine conditions as illustrated in Fig. S5D (dashed line vs. goldenrod line) (39). The hygroscopicity ( $\kappa$ ) value used for activation is 0.12, based on the measured hygroscopicity ( $\kappa$ ) for urban pollution during the 2014 wet season that is generally between 0.1- 0.15 for aerosols smaller than 100 nm (53). The aerosols are horizontally homogeneous over the domain. In this simulation, the aerosol plume was transported from the Manaus metropolis to the T3 site by the northeasterly wind at low levels, and Fig. S5B shows how the aerosol plume looks like at 12:00 UTC on 17 March (after 1-day simulation). The three-times-higher aerosol concentrations in the plume were based on the CCN measurements at the 0.23% supersaturation on the aircraft for this case, which shows about 2-4 times increase from the background to the plume conditions. Over the Amazon rainforest without disturbance by human activities (note this is different from the present background condition mentioned above), the aerosol concentration is close to a clean pre-industrial (PI) condition, and  $\text{UAP}_{<50}$  are very low in concentration due to the lack of particle nucleation events in the isoprene-dominated environment. Although convective downdraft transports small particles from the free troposphere, the particles grow to the size of the accumulation mode quickly (27). To mimic a PI condition without  $\text{UAP}_{<50}$  and isolate the contribution of  $\text{UAP}_{<50}$  that are produced by Manaus pollution plume to the increased convective intensity and precipitation from C\_BG to P3\_BG, we carried out another pair

of simulations, C\_PI and PL3\_PI based on C\_BG and P3\_BG, respectively, except that  $UAP_{<50}$  were removed in both background and plume conditions (Fig. S5D and Table 1).

The aerosol concentration was assumed to be uniform within 2 km above the ground and exponentially decrease above 2 km in the four main simulations in Table 1 (the first 4 simulations). A new observational study showed that aerosol concentration peaks at the upper troposphere over the Amazon region (46). To look at whether the high concentration of aerosols at upper levels could impact our results, we conducted sensitivity tests by using a similar vertical distribution (VD) as in Fig. 7b of ref. 46. That is, aerosol concentration is kept as a constant below 6 km (Fig. S6B), and an exponential increase from 6 to 11 km. Above 11 km, an exponential decrease is assumed. Two tests (C\_BG\_VD and C\_PI\_VD) were performed corresponding to the original simulations of C\_BG and C\_PI (Table 1), respectively, except using the new vertical distribution. The aerosol concentration below 6 km altitude in C\_BG\_VD and C\_PI\_VD is set to be the same as that of C\_BG and C\_PI, respectively. The highest concentration at upper levels is about 11 times larger than that below 6 km, consistent with Fig. 7b of ref. 46.

Aerosol SD could vary significantly. To examine if our conclusions are affected by a different SD, we performed sensitivity tests by employing a SD measured at about 20 km downwind of the Manaus city (Line 2 in Fig. S6C). Lines 3 and 4 are further downwind with Line 4 around the T3 area, where  $UAP_{<50}$  are much lower. Also, aerosols measured at these locations likely went through cloud processing because of cloud and precipitation occurring nearby. Thus, we chose Line 2 to represent the plume condition in the sensitivity tests. Three tests were conducted following the same setup as the previous simulations except for a different SD (Table 1): the plume case P3\_BG\_SD, the present-day background case C\_BG\_SD, and the PI case C\_PI\_SD (Fig. S6D). The total aerosol concentration of Line 2 is about  $1.14 \times 10^4 \text{ cm}^{-3}$ , which is very high due to contribution of  $UAP_{<50}$ .

Because all  $UAP_{<50}$  were removed in the PI condition to examine the contribution of  $UAP_{<50}$ , to show that our conclusion and the proposed mechanism are not impacted by a small amount of  $UAP_{<50}$  in the PI condition, we conducted an additional sensitivity test C\_PI2 (Table 1), in which  $60 \text{ cm}^{-3}$  of  $UAP_{<50}$  were added to the SD of C\_PI (Fig. S5D). The SD for C\_PI2 was based on measurements at the remote site Amazon Tall Tower Observatory (ATTO) in the central Amazon Basin (a present-day pristine condition, Fig. 6a of ref. 39) and scaled to a total  $N_a$  of  $190 \text{ cm}^{-3}$  with  $UAP_{<50}$  of about  $60 \text{ cm}^{-3}$ . This value of  $N_a$  is an approximated PI condition, which is at the low end of the range of observations under the present-day pristine conditions (35<sup>th</sup> percentile with regard to  $CCN_{>50}$ ) while the SD shape is similar to the average rainforest aerosol SD for both present-day pristine conditions (Fig. 6a in ref. 39) and the entire wet season (Fig. 6 of ref. 40). The hygroscopicity used is 0.12, the same as other simulations. It is shown that the small amount of  $UAP_{<50}$  only leads to about 4% increase in updraft strength (Fig. S16A) through a slightly decreased supersaturation above cloud base (Fig. S16B). This increase is negligible compared with the 80% increase from C\_PI to C\_BG, suggesting that we should expect the similarly large  $UAP_{<50}$  effects for a pristine area with a low  $UAP_{<50}$  concentration.

We also conducted the sensitivity tests C\_PI\_ATTO and C\_BG\_ATTO (Table 1) for testing the addition of  $\text{UAP}_{<50}$  to the present-day pristine  $\text{CCN}_{>50}$  condition. The size distributions for these simulations were based on C\_PI and C\_BG, respectively, with the mean number of  $\text{CCN}_{>50}$  ( $200 \text{ cm}^{-3}$ ) averaged over all measurements under present-day pristine conditions at the ATTO site (goldenrod line in Fig. S5D) (39). We see the similar  $\text{UAP}_{<50}$  effects on updraft velocity and supersaturation as shown in Fig. S17. Therefore, an addition of a descent amount of ultrafine particles to the present-day pristine conditions would also drastically invigorate DCCs.

In summary, we conducted the simulations for the addition of  $\text{UAP}_{<50}$  to the various  $\text{CCN}_{>50}$  conditions (i.e., an approximated PI condition, a present-day pristine condition, and a Manaus regional background condition). We show the similar convective invigoration by ultrafine particles through drastically reducing water supersaturation and forming additional cloud water and condensational heating in all the tested scenarios, mainly because of the strong capacity of these DCCs that develop in a humid condition in activating ultrafine particles.

It should be noted that the measured aerosol SD and VD employed the sensitivity tests were from a particular location, so we still have to assume uniform aerosol properties (i.e., SD, VD, and hygroscopicity) over the entire domain or over the entire plume area, which are still not the same as the reality. Thus, we used the idealized aerosol setup to understand the mechanism and isolate the contributions first, then showed that the mechanism is robust with various aerosol properties (i.e., SD, and VD) measured over the Amazon.

## **Supplementary Text**

### Baseline simulation evaluation

The baseline simulation P3\_BG was evaluated with available observations in meteorology, clouds, and precipitation. Fig. S7 shows that the simulated profiles of temperature, water vapor, and wind fields agreed well with sounding observations at the T3 site at 14:20 UTC. For cloud properties, the aircraft only sampled shallow warm clouds at flight levels around 1-km altitude between the Manaus metropolis and the T3 site; thus, the sampling was not representative of the deep convective clouds we analyzed around the T3 site. Due to limited sample size (less than 10 min in-cloud measurements) and large variability of the measured cloud droplet concentration ( $1\text{-}800 \text{ cm}^{-3}$ ) sampled by aircraft over a long distance, it was difficult to compare the data with the simulations. In general, the cloud droplet concentrations around cloud center at the 1-km altitude for the plume-affected region were  $200\text{-}600 \text{ cm}^{-3}$ , and the corresponding modeled values in P3\_BG were generally within that range. Again, these values were for the shallow clouds, not the deep convective clouds around the T3 site that we focused on in this study.

Fortunately, we had the S-band (SIPAM) and X-band radar measurements as reference for the deep convective cloud properties around the T3 site, although the radars had some missing data during the strong precipitation period between 1736-1824 UTC. Note, the RWP did observe the passage of a moderate convective cell at the T3 site during this

period, but it is difficult to compare column measurements with 3-D cloud simulations due to limited sampling over such a short time period (the temporal and spatial shifts of convection in the simulation further increased the difficulties to compare). We showed the comparison of the retrieved rain rate at around 18:24 UTC from SIPAM and X-band radar (estimated at the 2.5-km altitude) with that in P3\_BG (Fig. S8, PL3\_PI is plotted to show the impact of  $UAP_{<50}$ ). The SIPAM retrieved rain rates are generally larger than those estimated by the X-band radar, but both estimates show the rain core around the T3 site (already passed the T3 site by this time). The rain rate intensity from the rain core around the T3 site was well captured by P3\_BG, but significantly weaker in other three simulations (i.e., PL3\_PI, C\_PI, and C\_BG). The time series of the rain rate comparison as seen in Fig. S9A shows that the simulation with the Manaus pollution plume (P3\_BG) was able to reproduce the intensity and the timing of the peak rain rate from the rain core around the T3 site. The 10-dBZ echo top height from the simulated radar reflectivity for P3\_BG agreed well the SIPAM observations during the deep convection cloud period (i.e., after 1700 UTC; Fig. S9B), suggesting qualitatively that observed precipitation-sized particles being lofted to high altitudes by intense convective updrafts were reasonably captured by the simulation. All these evaluations indicate that the baseline simulation reasonably reproduced the convective intensity and precipitation of the locally occurring system around the T3 site.

#### Relative role of enhanced latent heating at low, middle and upper levels

As shown in Fig. 4B (third from top), the condensational heating is the dominant heat source at low and middle levels, whereas at upper levels it is the depositional heating. We conducted three sensitivity experiments based on P3\_BG to gain understanding of the relative role of the increased latent heat at low, middle, and upper levels in intensification of convection. In P3\_BG\_LH1, the net latent heat of condensation and evaporation in the warm phase (above 0 °C) was multiplied by a factor of 0.85. The factor means a 15% reduction from P3\_BG. In P3\_BG\_LH2, the latent heat at upper levels from the deposition, freezing including riming, and sublimation was reduced by 15% from P3\_BG. As shown Fig. 4B (third from top), the depositional heating is dominant and has large values at 8 to 11 km altitudes, so this test was to show the impact of increased latent heating at upper levels (a test by excluding the reduction in riming or drop freezing did not make much difference). At middle levels, condensational heating is dominant compared with other processes (Fig. 4B, third row). Therefore, in P3\_BG\_LH3, the net latent heat of condensation and evaporation is reduced by 15% at middle levels (-38 to 0 °C). Note, we reduced the cooling terms correspondingly to maintain the balance of the microphysical processes. For example, reducing latent heating from condensation by 15%, implies an unaccounted for increase of evaporative cooling.

Fig. S13A clearly shows that with a 15% reduction of the net latent heating at low levels, the convective intensity over the entire vertical profile was reduced drastically (purple vs. red in Fig. S13A). In contrast, with the same reduction at upper levels (e.g., mainly 8 to 11 km), the updraft velocity was decreased only above 8 km (green), with a magnitude of 50% smaller than the reduction found in P3\_BG\_LH1. With the reduction at middle levels (orange line), the magnitude of the reduced updraft velocity is similar to that of reducing latent heat at upper levels, which is much smaller than the impact of reducing

the low-level heating. The probability density function (PDF) of  $w$  in Fig. S14 shows similar results. Given the increase of the net latent heating at low levels from C\_PI to C\_BG averaged over the entire convection period (1400-2000 UTC) is 27%, doubled than that at upper levels (i.e., 14%), and the low levels were dominated by condensational latent heating, we concluded that the increase of condensational heating played the predominant role in the substantial enhancement of convection by  $UAP_{<50}$ , whereas the enhanced latent heating from ice-related processes at upper levels played a secondary role. The corresponding changes in precipitation are shown in Fig. S13B.



Table S1 Aerosol number concentrations for all 17 selected local occurring systems from 2014 wet season with  $D > 15$  nm and  $D > 50$  nm in the order of low to high concentrations as plotted in Fig. 2A.

Date (MM/DD)	$D > 15$ nm ( $\text{cm}^{-3}$ )	Date (MM/DD)	$D > 50$ nm ( $\text{cm}^{-3}$ )
03/23	495	03/22	287
03/22	553	03/23	302
04/21	609	04/21	353
05/31	711	05/16	383
05/30	853	05/30	449
04/12	1455	04/01	537
05/16	1525	05/31	649
05/19	1662	05/20	716
04/23	1721	04/23	793
04/18	1930	04/12	877
04/01	1998	04/18	952
03/11	2346	03/11	1079
05/20	2679	05/19	1214
03/26	3162	03/26	1348
04/20	3462	03/17	1664
03/17	3619	03/21	1872
03/21	3848	04/20	1927

Fig. S1. Vertical profile of PDF of the updraft speeds ( $w$ ;  $\text{m s}^{-1}$ ) in convective area for  $D > 15$  nm (left) and  $D > 50$  nm (right) for the four aerosol groups as in Fig. 2B. For each aerosol group, the frequency for  $w$  in each bin is calculated using an interval of  $1 \text{ m s}^{-1}$  with the number of points divided by the total convective points of the group (i.e., sum of the convective points from the cases of the group).

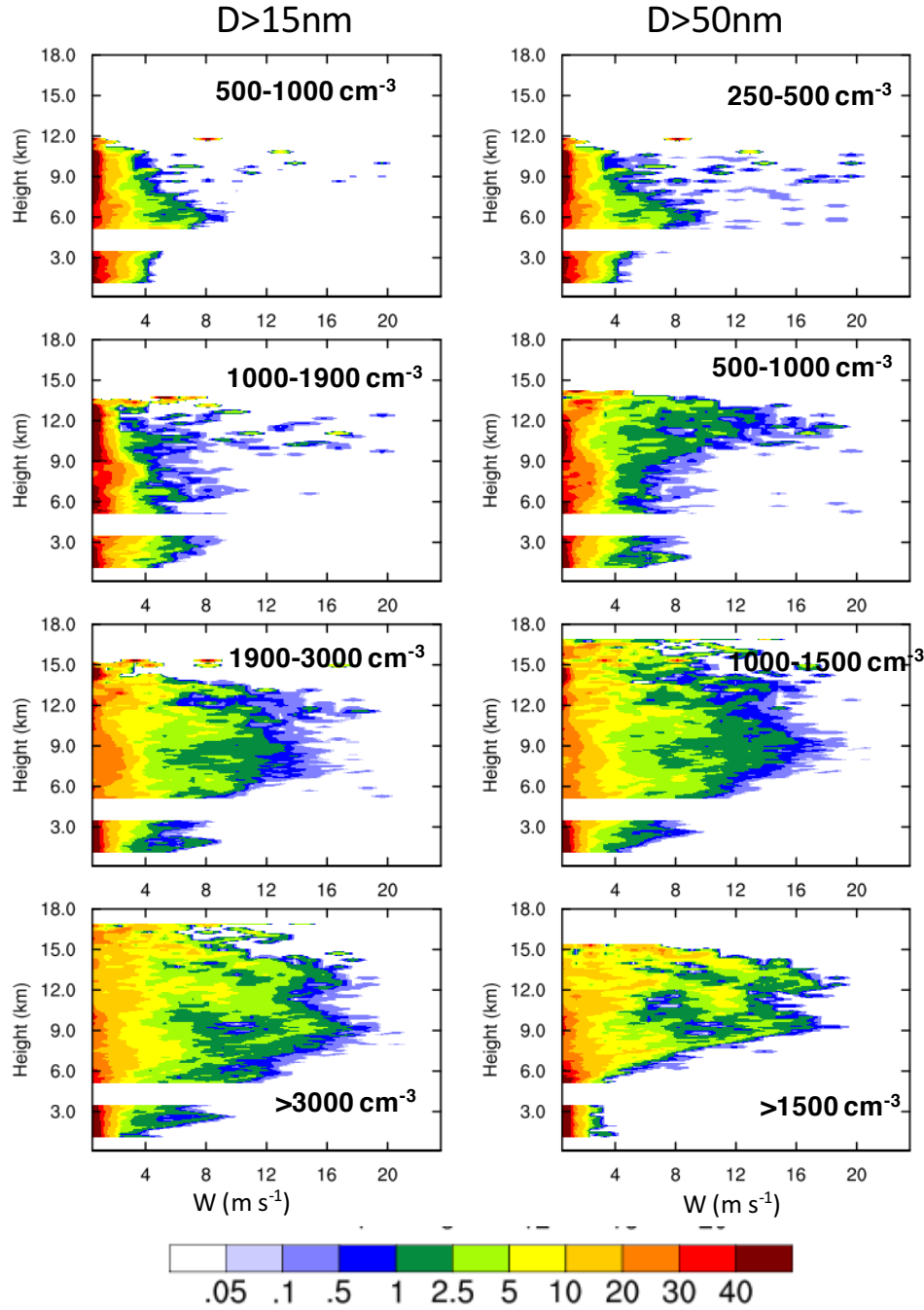


Fig. S2. Correlation of the maximum velocity averaged over the top 10 percentiles of updrafts in each case with aerosol concentrations for (A)  $D > 15$  nm and (B)  $D > 50$  nm. (A) shows  $R^2$  is doubled for aerosols with  $D > 15$  nm compared with that with  $D > 50$  nm, indicating that the correlation is higher for  $D > 15$  nm. However, the correlation for both  $D > 15$  nm and  $D > 50$  nm are not good because the data are too scattered and the single maximum of vertical velocity may not be representative of convective intensity. (C) and (D) are the PDFs of the surface rain rates stratified according to the four aerosol groups for  $D > 15$  nm and  $D > 50$  nm, respectively. The surface rain rates are the retrieved data based on reflectivity-based relationships from the RWP, an accurate surface rain rate measurement at very high temporal resolution within deep convective clouds. The frequency calculation is similar to that for  $w$  in Fig. S1, except that the rain rate PDF is calculated over the range of 0.25- 85 mm h<sup>-1</sup> evenly separated into 15 bins. (C) clearly shows that the maximum rain rates get larger as  $N_a$  with  $UAP_{<50}$  increases (i.e., the largest rain rate bin is 60-66, 66-72, 72-78, and 78-84 mm/h from the low- $N_a$  to high low- $N_a$  groups for  $D > 15$  nm).

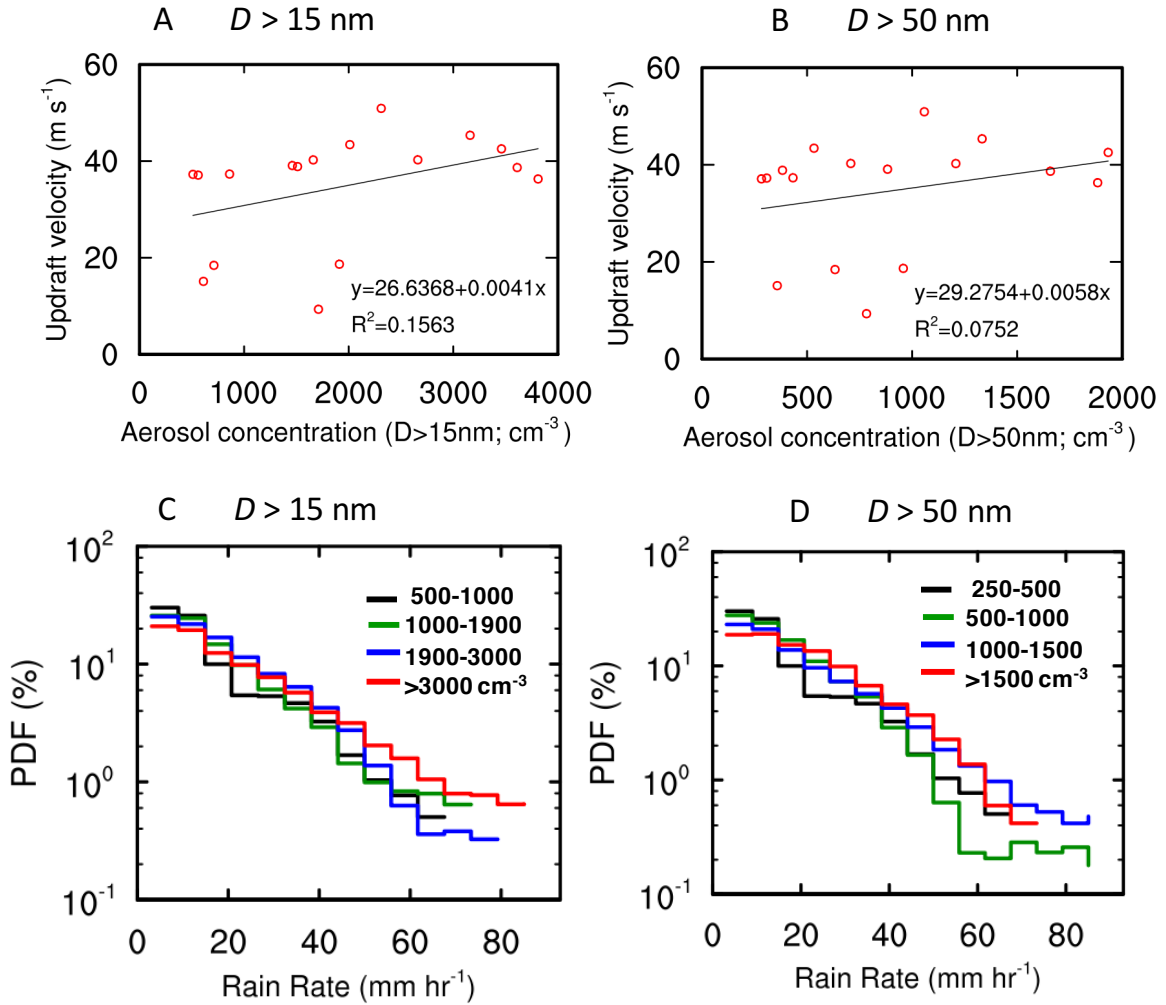


Fig. S3. Vertical profiles of temperature, RH, zonal U- and meridional V-winds stratified according to the four aerosol groups for  $D > 15$  nm. The data are from the nearest sounding before the convection event for each case (the same data used for CAPE and CIN calculations in Fig. 2A).

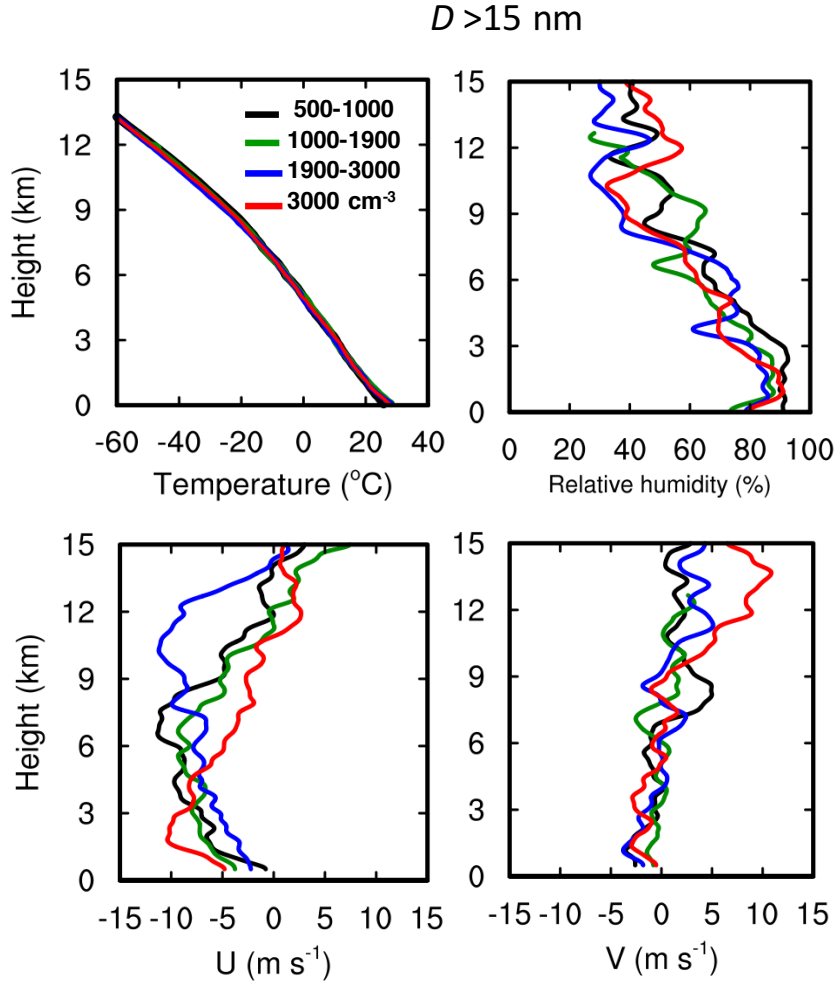


Fig. S4. The case for model study. (A) The composite radar reflectivity (i.e., the column maximum) from the SIPAM radar at 18:24 UTC 17 March 2014. T1 is a research site in the Manaus metropolis, and T2 is just downwind of the Manaus metropolis. T3 is the location of the RWP and 70-km downwind of the Manaus metropolis. (B) Skew-T plot for the sounding data at 14:20 UTC at the T3 site.

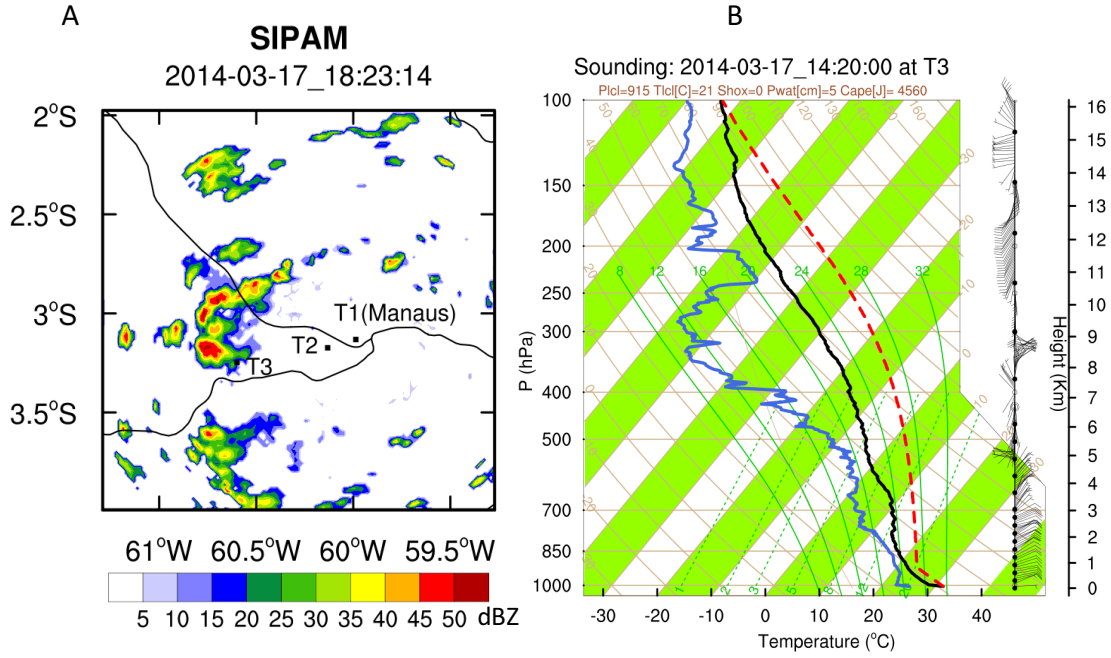


Fig. S5. (A) The simulation Domain 1 (d01) and Domain 2 (d02), (B) aerosol concentrations after 1-d simulation in P3\_BG (the black box is the Manaus metropolis, where the aerosol plume was imposed). See Fig. S4A caption about T1, T2, and T3. (C) Initial aerosol size distribution for C\_BG (solid blue) P3\_BG (solid red), C\_PI (dashed blue), and PL3\_PI (dashed red). (D) The size distribution for the sensitivity test C\_PI2 (solid grey) that has a small amount of  $\text{UAP}_{<50}$ , i.e., adding  $60 \text{ cm}^{-3} \text{ UAP}_{<50}$  to C\_PI, and the sensitivity test C\_PI\_ATTO (solid goldenrod) in which the value of  $\text{CCN}_{>50}$  was taken from the average measurements at ATTO for the entire wet season.

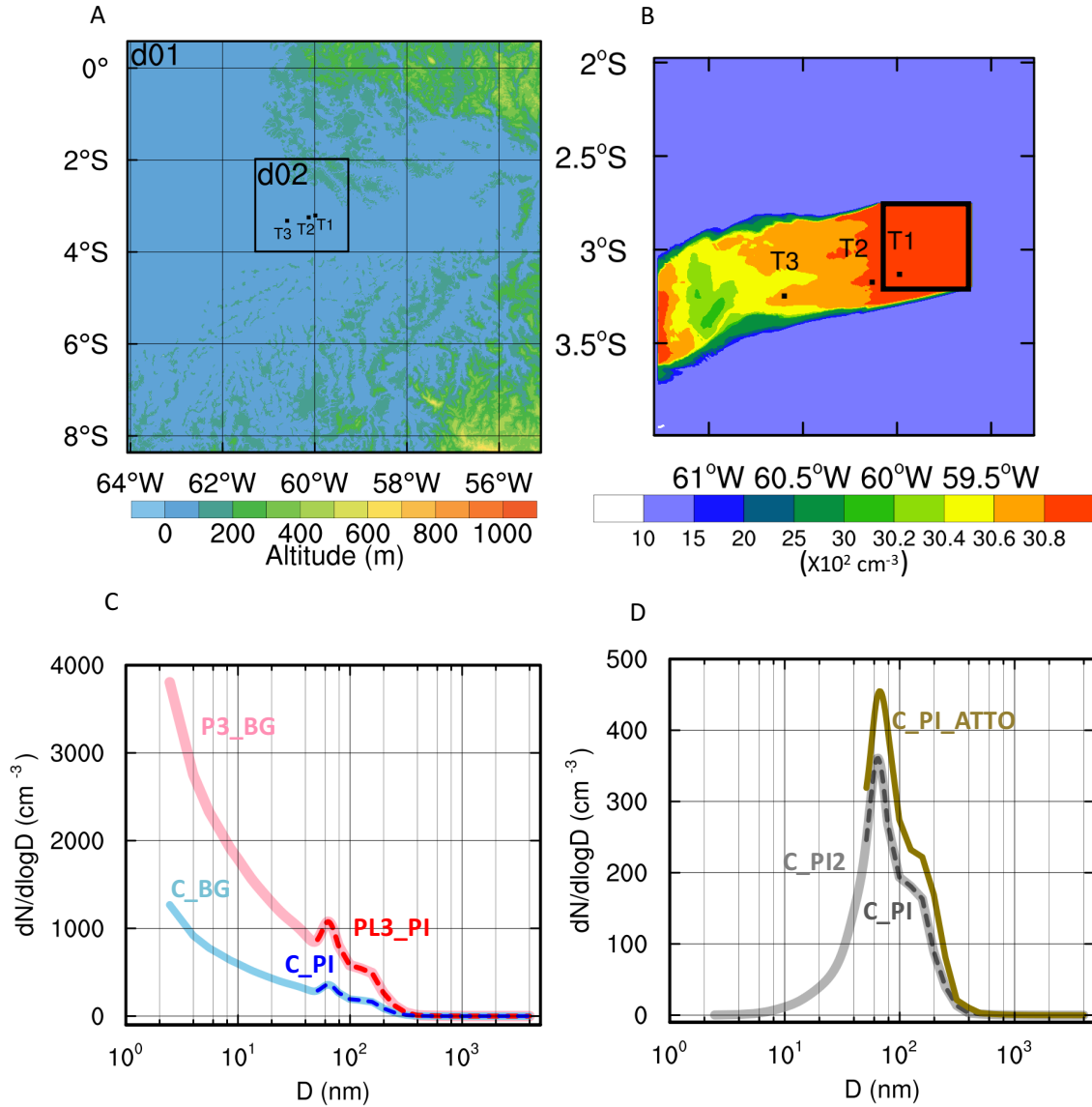


Fig. S6 Aerosol vertical distribution (VD) for (A) C\_PI (dashed) and C\_BG (solid), and (B) the tested VD in C\_PI\_VD (dashed) and C\_BG\_VD (solid). (C) The observed aerosol size distribution (SD) from the FIMS measurements on aircraft. Line 1 is for the location of inside Manaus. Lines 2, 3, and 4 are for the locations of 20 km, 40 km, and 70 km downwind Manaus, respectively. Line 4 is near T3. (D) The tested SD in the plume case P3\_BG\_SD (light blue, similar to Line 2 in C), the present background case C\_BG\_SD (orange), and the pre-industrial case C\_PI\_SD (brown).

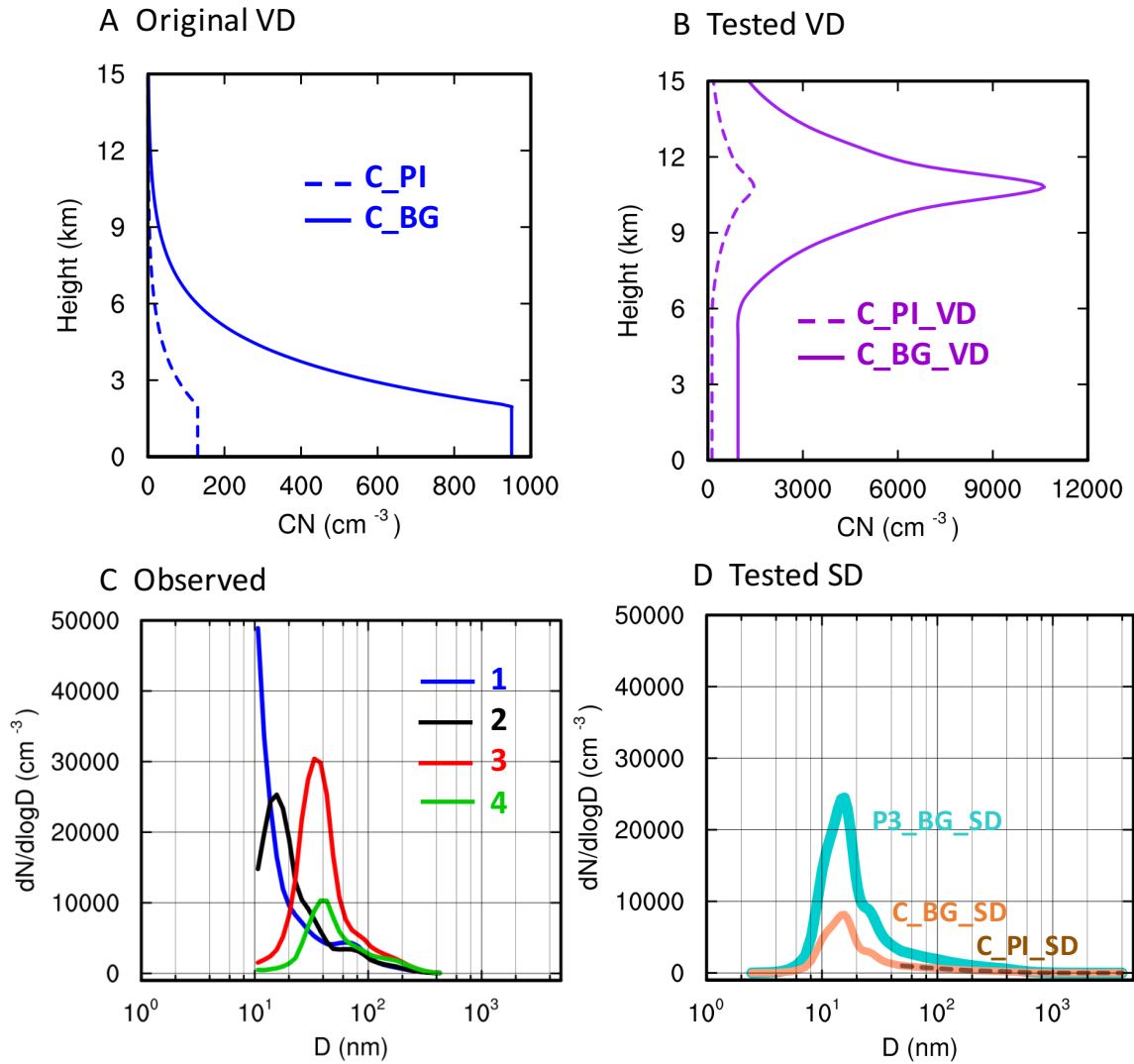


Fig. S7. Comparison of the temperature, RH, U- and V-winds from the sounding data at 14:20 UTC at the T3 site (circle) with those from the same time and location in P3\_BG (red).

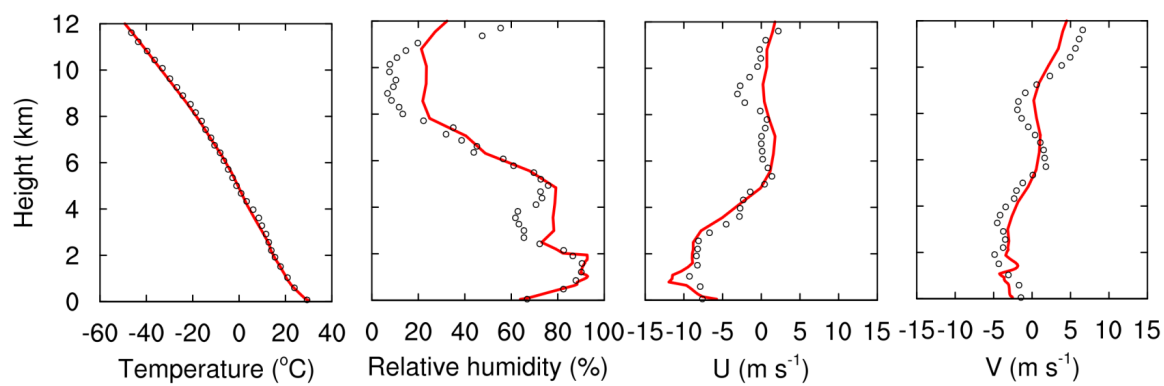




Fig. S8. Rain rate at 2.5-km altitude from SIPAM, X-band radar, P3\_BG, and PL3\_PI. The red box is where the observed deep convective event resides, and is the analysis area of this study for the plume-affected deep convective cloud systems. The modeled rain rates are also from the 2.5-km altitude and an approximately 20-min time shift is considered based on the time series of rain rate plot in Fig. S9A. The domain shown here is smaller than the modeled domain. Comparison of P3\_BG with PL3\_PI shows the addition of  $UAP_{<50}$  to the plume and background area greatly enhances rain rate not only in the plume-affected area (i.e., around the T3 site) but also in the whole domain.

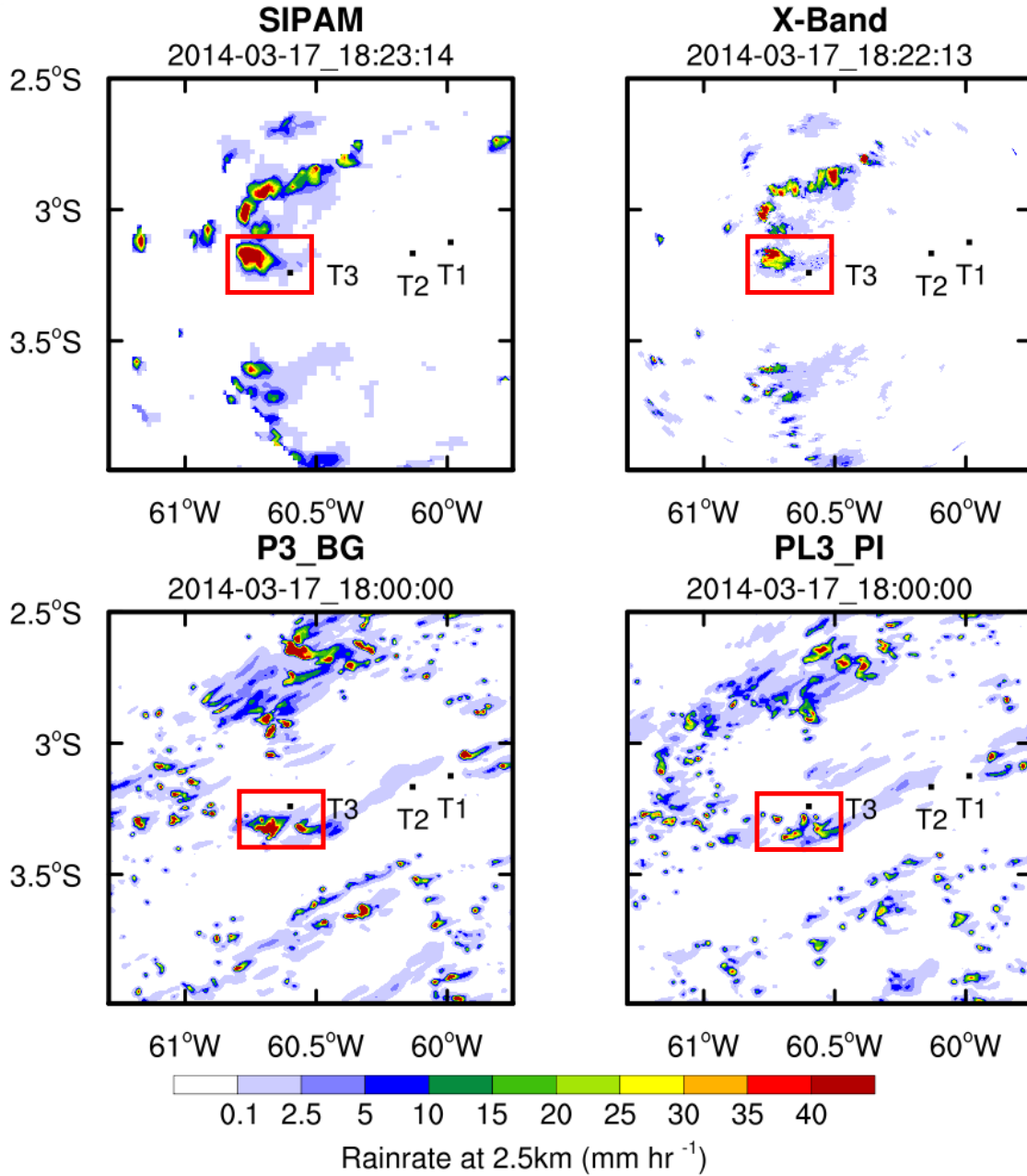


Fig. S9. Time series of (A) rain rate at 2.5-km altitude from SIPAM, X-band radar, P3\_BG, and PL3\_PI, and (B) the 10-dBZ echo top height from SIPAM, P3\_BG, and PL3\_PI. The comparison is based on the convective system around the T3 site (red box in Fig. S8). The radar data were missing during the strong precipitation period between 1736-1824 UTC. The 10-dBZ echo top height might not be accurate for shallow clouds so the comparison is shown for 1800-2000 UTC.

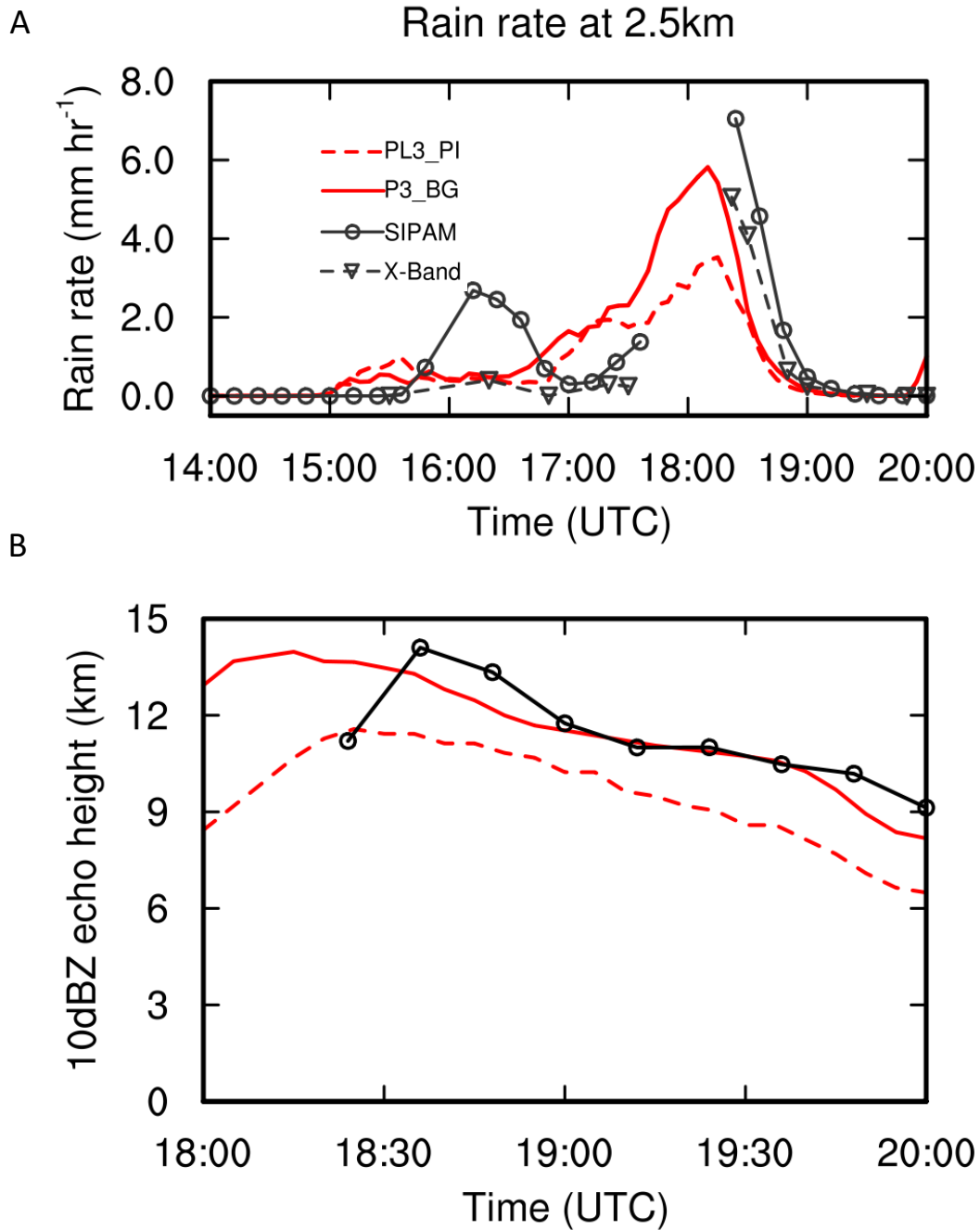


Fig. S10. Vertical profile of PDF of updraft speeds for  $w > 2 \text{ m s}^{-1}$  from C\_PI, PL3\_PI, C\_BG, and P3\_BG during 1400-1900 UTC from the deep convective clouds around the T3 site (red box in Fig. S8). The frequency calculation for each level is based on  $w$  ranging from 2 to  $24 \text{ m s}^{-1}$  with  $0.1 \text{ m s}^{-1}$  intervals.

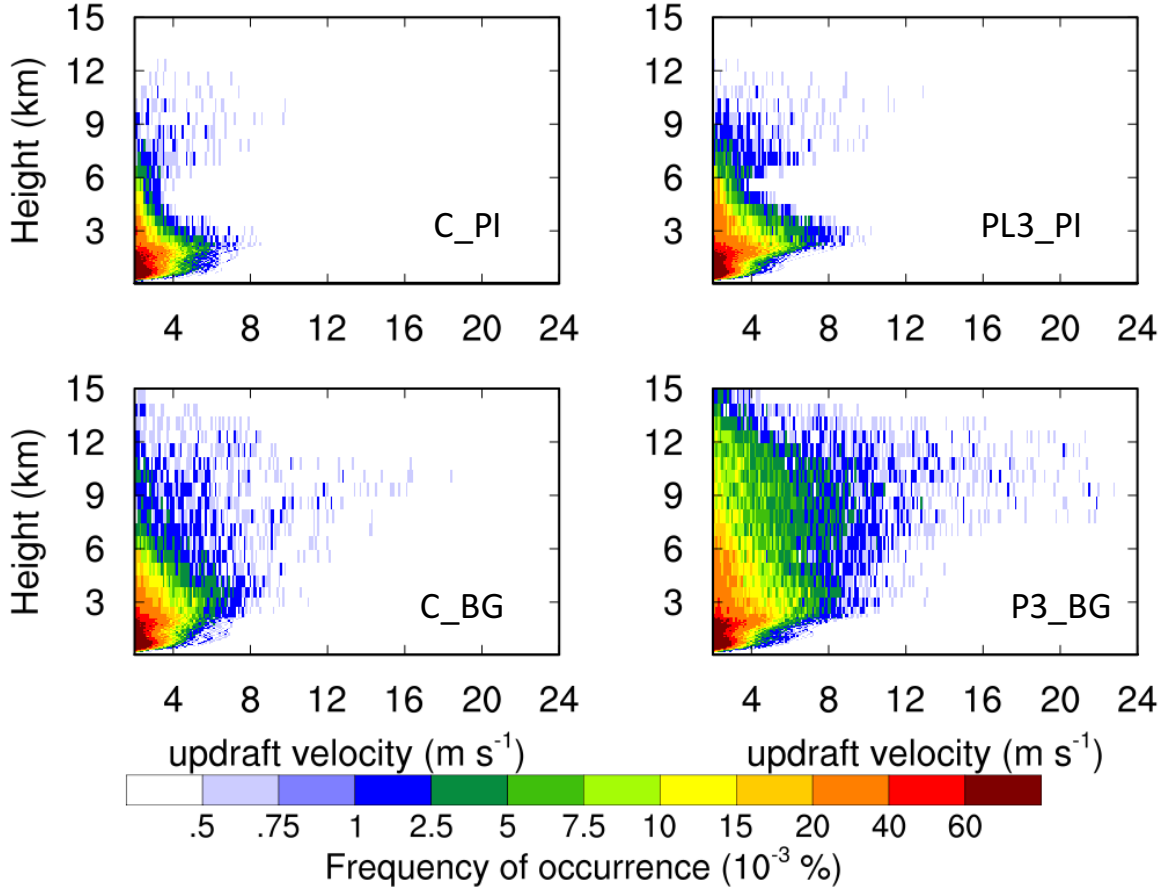


Fig. S11. Same as Fig. S10, except for over the entire domain.

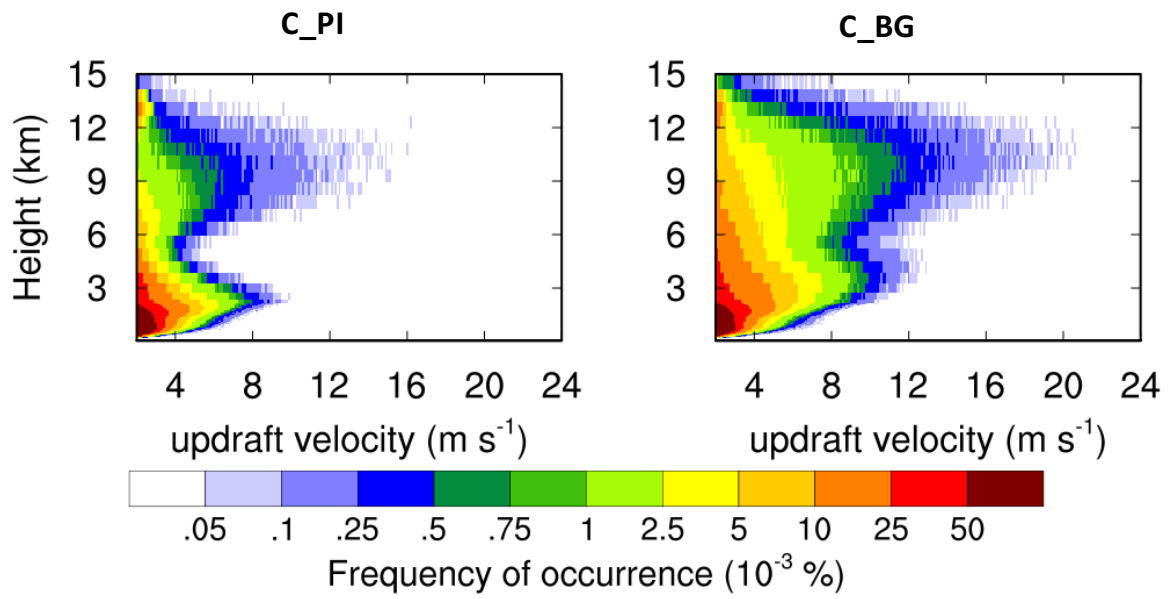


Fig. S12 (A) Same as Fig. 4, except for the net latent heat (heating + cooling) for the warm-cloud period (left) and deep-cloud period (right) in C\_PI (dashed) and C\_BG (solid), and (B) the mass (left) and number (right) concentrations of ice (green), now (blue), and graupel (red) at the deep-cloud period for C\_PI (dashed) and C\_BG (solid). The data were processed in the same way as Fig. 4B.

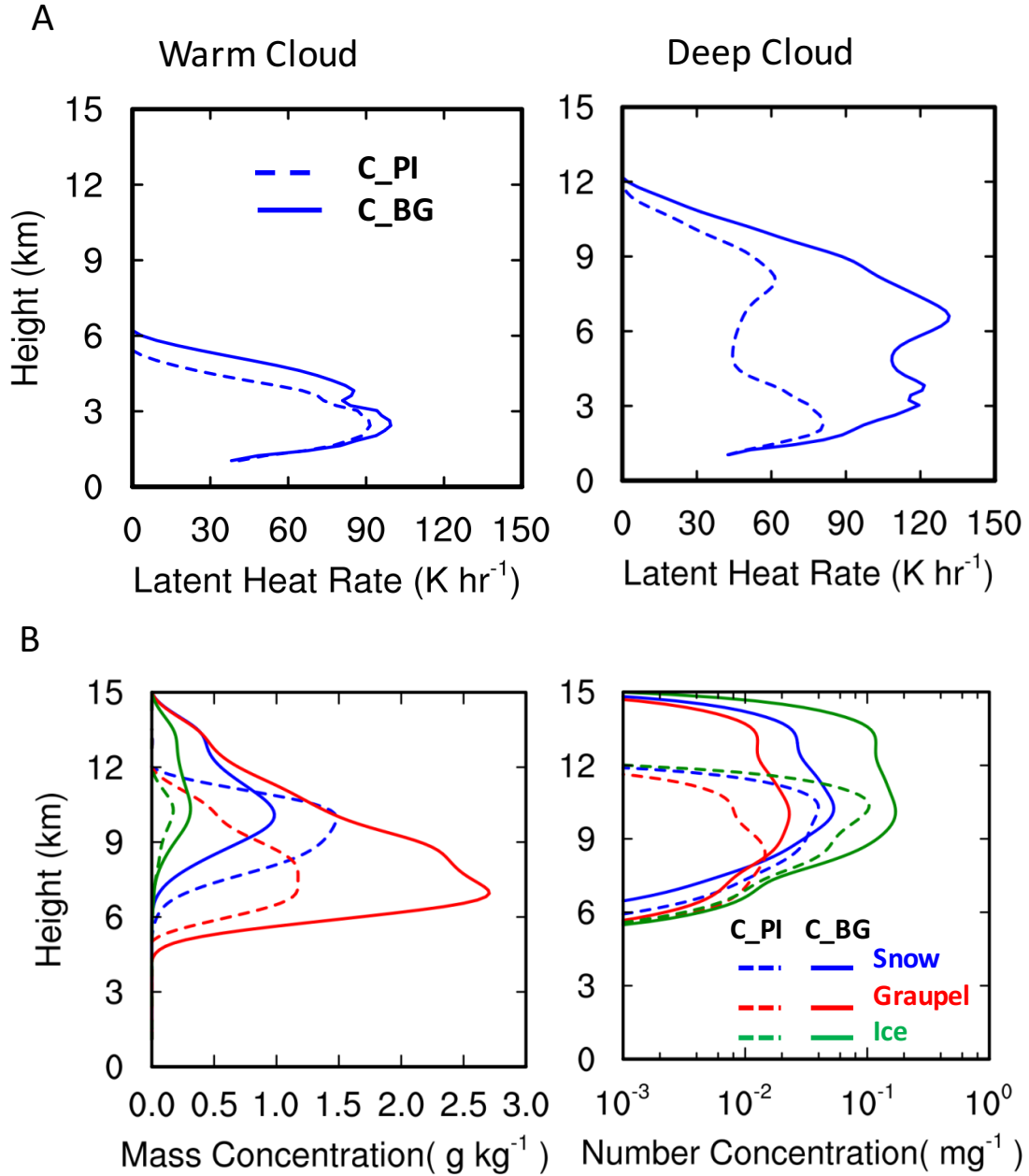


Fig. S13. Same as Fig. 3, except for (A) updraft velocity and (B) surface rain rate from P3\_BG (red solid), P3\_BG\_LH1 (purple solid), and P3\_BG\_LH2 (green), and P3\_BG\_LH3 (orange).

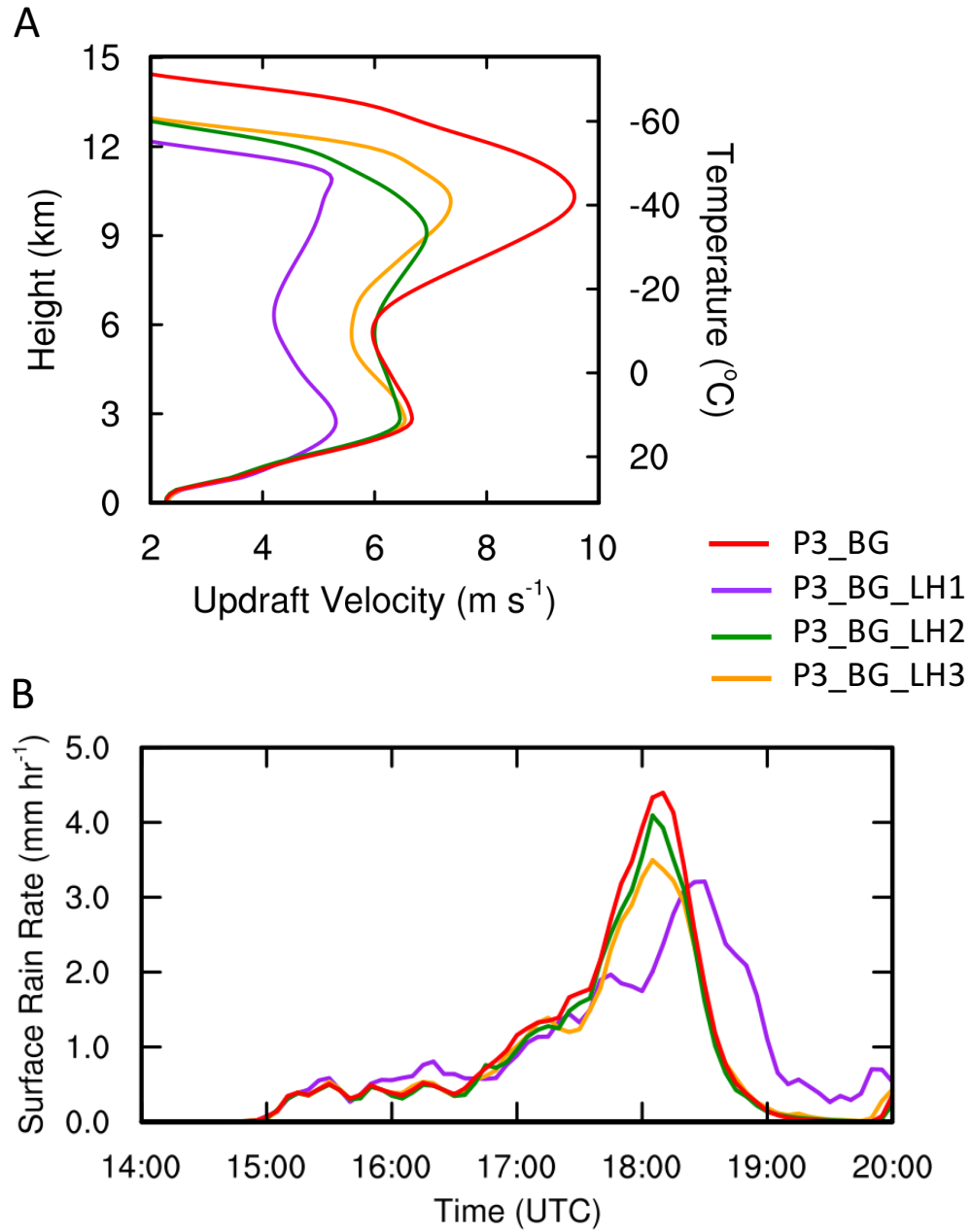


Fig. S14. Same as Fig. S10, except for P3\_BG, P3\_BG\_LH1, and P3\_BG\_LH2, and P3\_BG\_LH3.

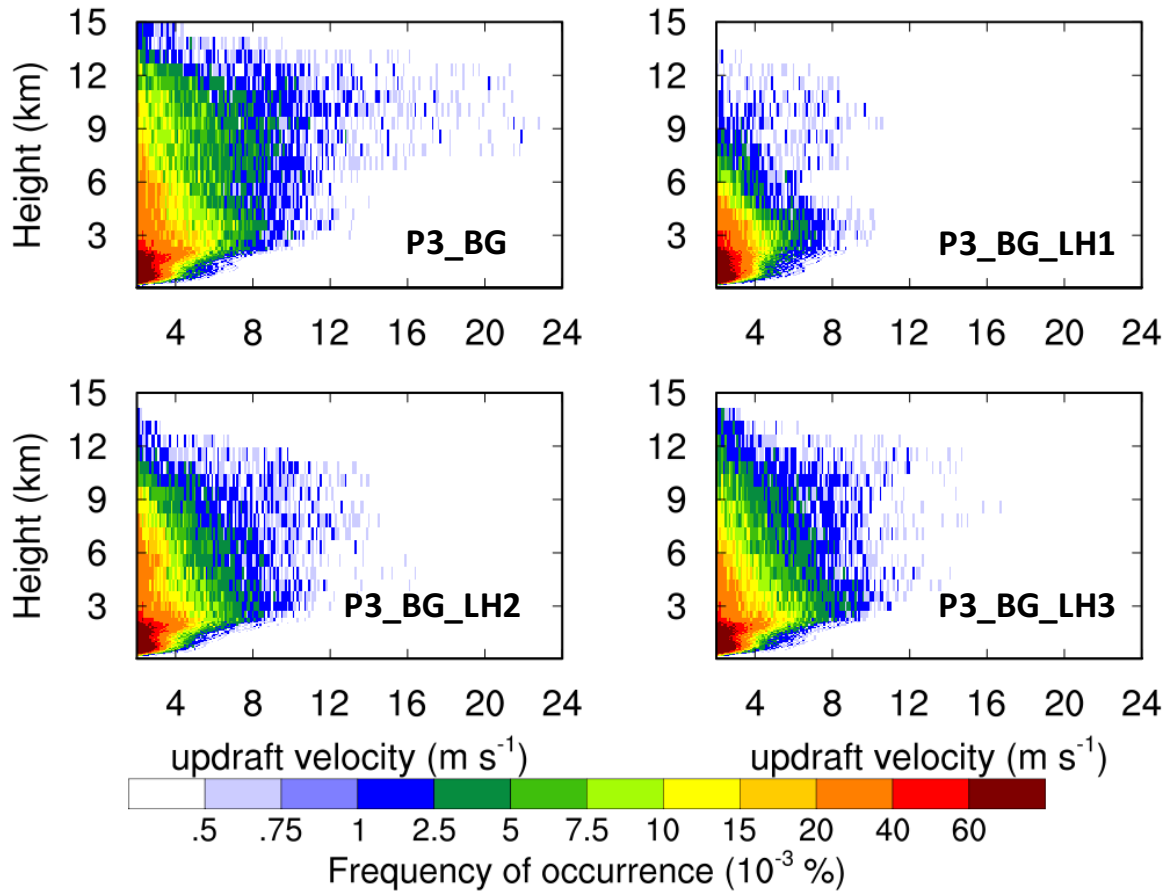


Fig. S15. The updraft velocity (A, C) and vapor supersaturation (B, D) for the sensitivity tests of aerosol vertical distribution (top) and size distribution (bottom). The results for vertical velocity were processed in the same way as Fig. 3A. Vapor supersaturation was processed in the same way as Fig. 4B.

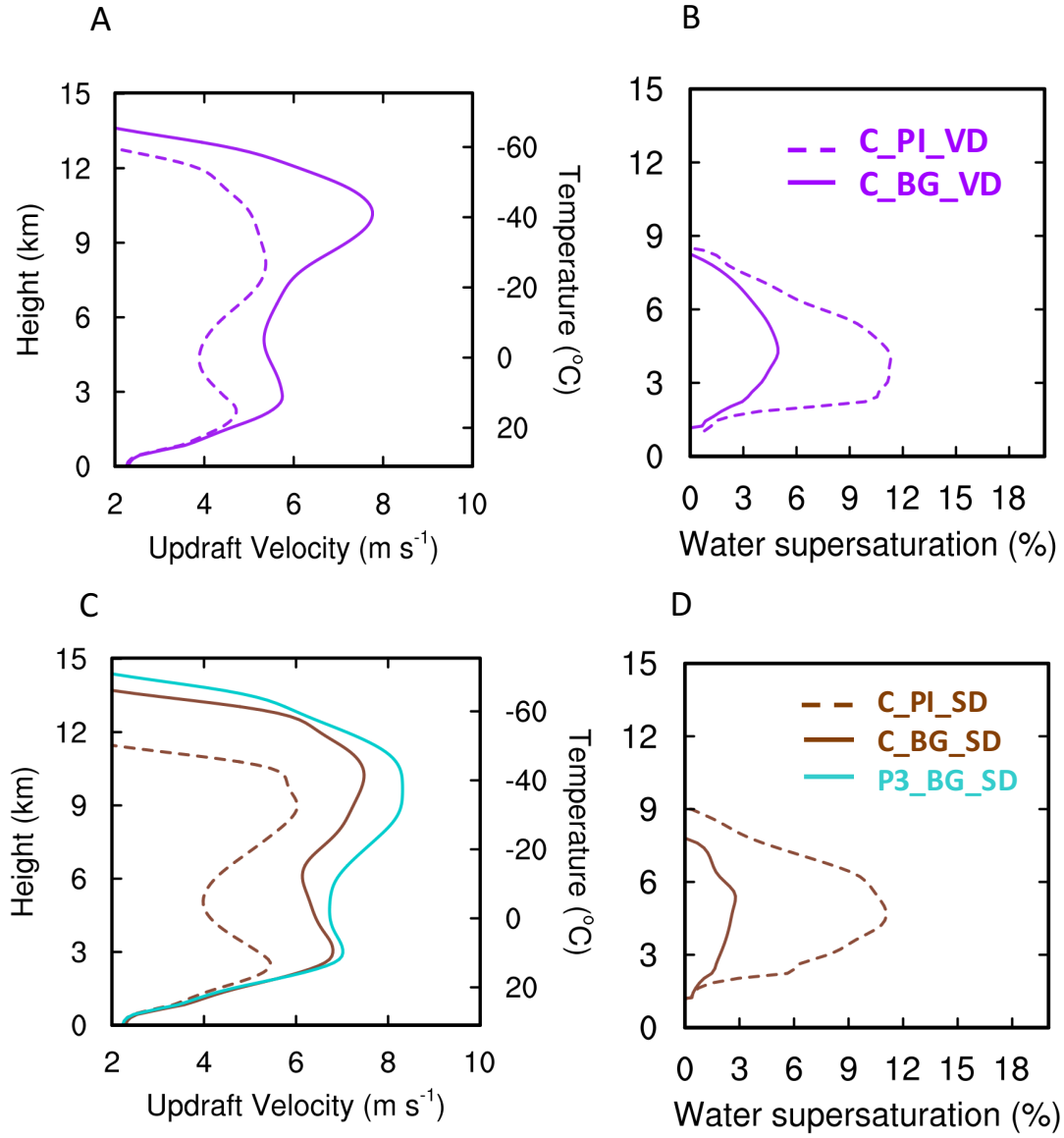




Fig. S16. Comparison of (A) updraft velocity, and (B) the corresponding vapor supersaturation (grey) and droplet nucleation rate (pink) between C\_PI and C\_PI2. Updraft velocity was processed in the same way as Fig. 3A, and vapor supersaturation and droplet nucleation rate were processed in the same way as Fig. 4B.

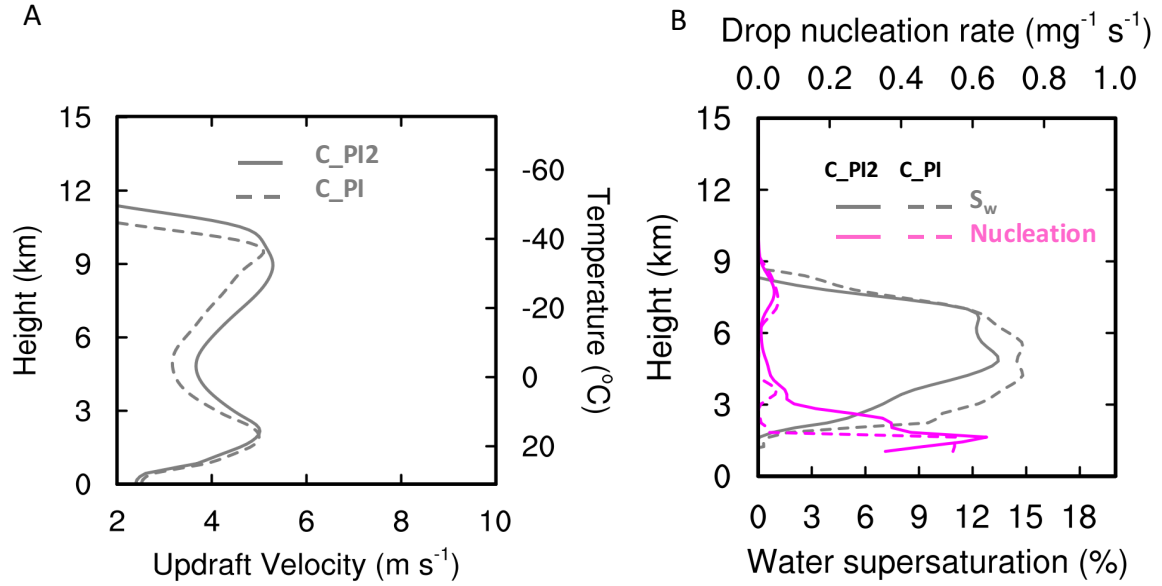
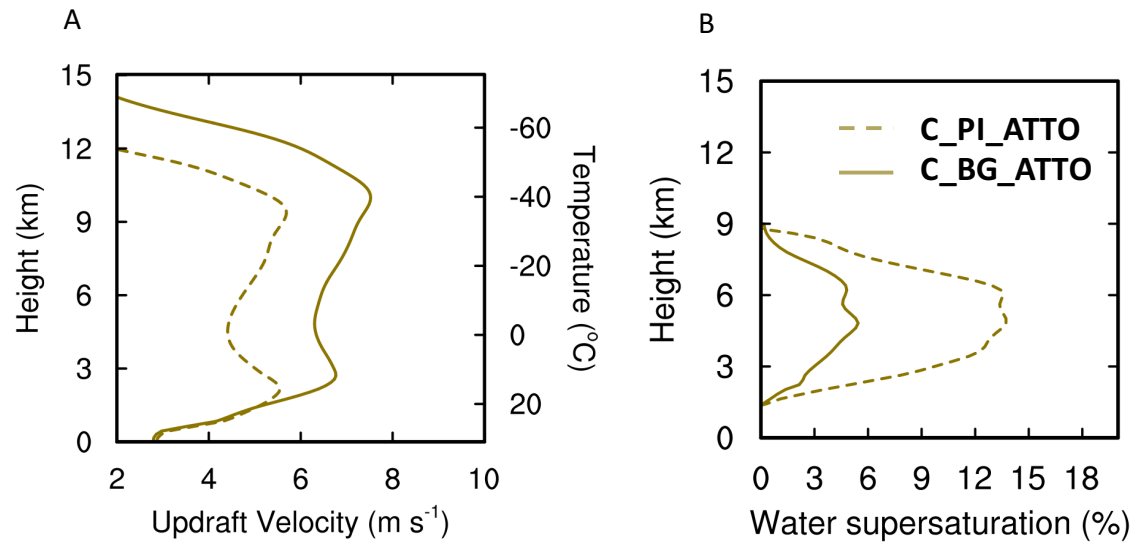


Fig. S17 (A) updraft velocity and (B) vapor supersaturation for the sensitivity tests of  $C_{PI\_ATTO}$  and  $C_{BG\_ATTO}$ . The results for vertical velocity were processed in the same way as Fig. 3A. Vapor supersaturation was processed in the same way as Fig. 4B



## References

1. R. A. Houze Jr., *Cloud Dynamics* (Elsevier/Academic Press, ed. 2, 2014).
2. H. C. Barnes, R. A. Houze Jr., Comparison of observed and simulated spatial patterns of ice microphysical processes in tropical oceanic mesoscale convective systems. *J. Geophys. Res. Atmos.* **121**, 8269–8296 (2016). [doi:10.1002/2016JD025074](https://doi.org/10.1002/2016JD025074)
3. *Climate Change 2013: The Physical Science Basis. Contribution of Working Group I to the Fifth Assessment Report of the Intergovernmental Panel on Climate Change* (Cambridge Univ. Press, 2013).
4. J. Fan, Y. Wang, D. Rosenfeld, X. Liu, Review of aerosol-cloud interactions: Mechanisms, significance, and challenges. *J. Atmos. Sci.* **73**, 4221–4252 (2016). [doi:10.1175/JAS-D-16-0037.1](https://doi.org/10.1175/JAS-D-16-0037.1)
5. W. K. Tao, J. P. Chen, Z. Li, C. Wang, C. Zhang, Impact of aerosols on convective clouds and precipitation. *Rev. Geophys.* **50**, RG2001 (2012). [doi:10.1029/2011RG000369](https://doi.org/10.1029/2011RG000369)
6. A. P. Khain, Notes on state-of-the-art investigations of aerosol effects on precipitation: A critical review. *Environ. Res. Lett.* **4**, 015004 (2009). [doi:10.1088/1748-9326/4/1/015004](https://doi.org/10.1088/1748-9326/4/1/015004)
7. S. S. Lee, L. J. Donner, V. T. J. Phillips, Y. Ming, The dependence of aerosol effects on clouds and precipitation on cloud-system organization, shear and stability. *J. Geophys. Res.* **113**, D16202 (2008). [doi:10.1029/2007JD009224](https://doi.org/10.1029/2007JD009224)
8. Z. J. Lebo, J. H. Seinfeld, Theoretical basis for convective invigoration due to increased aerosol concentration. *Atmos. Chem. Phys.* **11**, 5407–5429 (2011). [doi:10.5194/acp-11-5407-2011](https://doi.org/10.5194/acp-11-5407-2011)
9. R. L. Storer, S. C. van den Heever, Microphysical processes evident in aerosol forcing of tropical deep convective clouds. *J. Atmos. Sci.* **70**, 430–446 (2013). [doi:10.1175/JAS-D-12-076.1](https://doi.org/10.1175/JAS-D-12-076.1)
10. S. C. van den Heever, G. L. Stephens, N. B. Wood, Aerosol indirect effects on tropical convection characteristics under conditions of radiative-convective equilibrium. *J. Atmos. Sci.* **68**, 699–718 (2011). [doi:10.1175/2010JAS3603.1](https://doi.org/10.1175/2010JAS3603.1)
11. Z. Li, F. Niu, J. Fan, Y. Liu, D. Rosenfeld, Y. Ding, Long-term impacts of aerosols on the vertical development of clouds and precipitation. *Nat. Geosci.* **4**, 888–894 (2011). [doi:10.1038/ngeo1313](https://doi.org/10.1038/ngeo1313)
12. X. Yang, Z. Li, Increases in thunderstorm activity and relationships with air pollution in southeast China. *J. Geophys. Res. Atmos.* **119**, 1835–1844 (2014). [doi:10.1002/2013JD021224](https://doi.org/10.1002/2013JD021224)

13. D. Rosenfeld, U. Lohmann, G. B. Raga, C. D. O'Dowd, M. Kulmala, S. Fuzzi, A. Reissell, M. O. Andreae, Flood or drought: How do aerosols affect precipitation? *Science* **321**, 1309–1313 (2008). [doi:10.1126/science.1160606](https://doi.org/10.1126/science.1160606) [Medline](#)
14. A. P. Khain, V. Phillips, N. Benmoshe, A. Pokrovsky, The role of small soluble aerosols in the microphysics of deep maritime clouds. *J. Atmos. Sci.* **69**, 2787–2807 (2012). [doi:10.1175/2011JAS3649.1](https://doi.org/10.1175/2011JAS3649.1)
15. Q. Chen, I. Koren, O. Altaratz, R. H. Heiblum, G. Dagan, L. Pinto, How do changes in warm-phase microphysics affect deep convective clouds? *Atmos. Chem. Phys.* **17**, 9585–9598 (2017). [doi:10.5194/acp-17-9585-2017](https://doi.org/10.5194/acp-17-9585-2017)
16. J. Fan, L. R. Leung, D. Rosenfeld, Q. Chen, Z. Li, J. Zhang, H. Yan, Microphysical effects determine macrophysical response for aerosol impacts on deep convective clouds. *Proc. Natl. Acad. Sci. U.S.A.* **110**, E4581–E4590 (2013). [doi:10.1073/pnas.1316830110](https://doi.org/10.1073/pnas.1316830110)
17. U. Pöschl, S. T. Martin, B. Sinha, Q. Chen, S. S. Gunthe, J. A. Huffman, S. Borrmann, D. K. Farmer, R. M. Garland, G. Helas, J. L. Jimenez, S. M. King, A. Manzi, E. Mikhailov, T. Pauliquevis, M. D. Petters, A. J. Prenni, P. Roldin, D. Rose, J. Schneider, H. Su, S. R. Zorn, P. Artaxo, M. O. Andreae, Rainforest aerosols as biogenic nuclei of clouds and precipitation in the Amazon. *Science* **329**, 1513–1516 (2010). [doi:10.1126/science.1191056](https://doi.org/10.1126/science.1191056) [Medline](#)
18. M. O. Andreae, Aerosols before pollution. *Science* **315**, 50–51 (2007). [doi:10.1126/science.1136529](https://doi.org/10.1126/science.1136529) [Medline](#)
19. S. T. Martin, M. O. Andreae, D. Althausen, P. Artaxo, H. Baars, S. Borrmann, Q. Chen, D. K. Farmer, A. Guenther, S. S. Gunthe, J. L. Jimenez, T. Karl, K. Longo, A. Manzi, T. Müller, T. Pauliquevis, M. D. Petters, A. J. Prenni, U. Pöschl, L. V. Rizzo, J. Schneider, J. N. Smith, E. Swietlicki, J. Tota, J. Wang, A. Wiedensohler, S. R. Zorn, An overview of the Amazonian Aerosol Characterization Experiment 2008 (AMAZE-08). *Atmos. Chem. Phys.* **10**, 11415–11438 (2010). [doi:10.5194/acp-10-11415-2010](https://doi.org/10.5194/acp-10-11415-2010)
20. U. Lohmann, J. Feichter, Global indirect aerosol effects: A review. *Atmos. Chem. Phys.* **5**, 715–737 (2005). [doi:10.5194/acp-5-715-2005](https://doi.org/10.5194/acp-5-715-2005)
21. I. Koren, G. Dagan, O. Altaratz, From aerosol-limited to invigoration of warm convective clouds. *Science* **344**, 1143–1146 (2014). [doi:10.1126/science.1252595](https://doi.org/10.1126/science.1252595) [Medline](#)
22. M. O. Andreae, D. Rosenfeld, P. Artaxo, A. A. Costa, G. P. Frank, K. M. Longo, M. A. Silva-Dias, Smoking rain clouds over the Amazon. *Science* **303**, 1337–1342 (2004). [doi:10.1126/science.1092779](https://doi.org/10.1126/science.1092779) [Medline](#)
23. I. Koren, J. V. Martins, L. A. Remer, H. Afargan, Smoke invigoration versus inhibition of clouds over the Amazon. *Science* **321**, 946–949 (2008). [doi:10.1126/science.1159185](https://doi.org/10.1126/science.1159185) [Medline](#)

24. J. C. Lin, T. Matsui, R. A. Pielke Sr., C. Kummerow, Effects of biomass-burning-derived aerosols on precipitation and clouds in the Amazon Basin: A satellite-based empirical study. *J. Geophys. Res.* **111**, D19204 (2006). [doi:10.1029/2005JD006884](https://doi.org/10.1029/2005JD006884)
25. J. C. Zhou, E. Swietlicki, H. C. Hansson, P. Artaxo, Submicrometer aerosol particle size distribution and hygroscopic growth measured in the Amazon rain forest during the wet season. *J. Geophys. Res.* **107**, 8055 (2002). [doi:10.1029/2000JD000203](https://doi.org/10.1029/2000JD000203)
26. M. Kulmala, A. Asmi, H. K. Lappalainen, U. Baltensperger, J.-L. Brenguier, M. C. Facchini, H.-C. Hansson, Ø. Hov, C. D. O'Dowd, U. Pöschl, A. Wiedensohler, R. Boers, O. Boucher, G. de Leeuw, H. A. C. Denier van der Gon, J. Feichter, R. Krejci, P. Laj, H. Lihavainen, U. Lohmann, G. McFiggans, T. Mentel, C. Pilinis, I. Riipinen, M. Schulz, A. Stohl, E. Swietlicki, E. Vignati, C. Alves, M. Amann, M. Ammann, S. Arabas, P. Artaxo, H. Baars, D. C. S. Beddows, R. Bergström, J. P. Beukes, M. Bilde, J. F. Burkhardt, F. Canonaco, S. L. Clegg, H. Coe, S. Crumeyrolle, B. D'Anna, S. Decesari, S. Gilardoni, M. Fischer, A. M. Fjaeraa, C. Fountoukis, C. George, L. Gomes, P. Halloran, T. Hamburger, R. M. Harrison, H. Herrmann, T. Hoffmann, C. Hoose, M. Hu, A. Hyvärinen, U. Hörrak, Y. Iinuma, T. Iversen, M. Josipovic, M. Kanakidou, A. Kiendler-Scharr, A. Kirkevåg, G. Kiss, Z. Klimont, P. Kolmonen, M. Komppula, J.-E. Kristjánsson, L. Laakso, A. Laaksonen, L. Labonnote, V. A. Lanz, K. E. J. Lehtinen, L. V. Rizzo, R. Makkonen, H. E. Manninen, G. McMeeking, J. Merikanto, A. Minikin, S. Mirme, W. T. Morgan, E. Nemitz, D. O'Donnell, T. S. Panwar, H. Pawlowska, A. Petzold, J. J. Pienaar, C. Pio, C. Plass-Duelmer, A. S. H. Prévôt, S. Pryor, C. L. Reddington, G. Roberts, D. Rosenfeld, J. Schwarz, Ø. Seland, K. Sellegri, X. J. Shen, M. Shiraiwa, H. Siebert, B. Sierau, D. Simpson, J. Y. Sun, D. Topping, P. Tunved, P. Vaattovaara, V. Vakkari, J. P. Veefkind, A. Visschedijk, H. Vuollekoski, R. Vuolo, B. Wehner, J. Wildt, S. Woodward, D. R. Worsnop, G.-J. van Zadelhoff, A. A. Zardini, K. Zhang, P. G. van Zyl, V.-M. Kerminen, K. S. Carslaw, S. N. Pandis, General overview: European Integrated project on Aerosol Cloud Climate and Air Quality interactions (EUCAARI) – integrating aerosol research from nano to global scales. *Atmos. Chem. Phys.* **11**, 13061–13143 (2011). [doi:10.5194/acp-11-13061-2011](https://doi.org/10.5194/acp-11-13061-2011)
27. J. Wang, R. Krejci, S. Giangrande, C. Kuang, H. M. J. Barbosa, J. Brito, S. Carbone, X. Chi, J. Comstock, F. Ditas, J. Lavric, H. E. Manninen, F. Mei, D. Moran-Zuloaga, C. Pöhlker, M. L. Pöhlker, J. Saturno, B. Schmid, R. A. F. Souza, S. R. Springston, J. M. Tomlinson, T. Toto, D. Walter, D. Wimmer, J. N. Smith, M. Kulmala, L. A. T. Machado, P. Artaxo, M. O. Andreae, T. Petäjä, S. T. Martin, Amazon boundary layer aerosol concentration sustained by vertical transport during rainfall. *Nature* **539**, 416–419 (2016). [doi:10.1038/nature19819](https://doi.org/10.1038/nature19819) [Medline](#)
28. M. Pikridas, J. Sciare, F. Freutel, S. Crumeyrolle, S.-L. von der Weiden-Reinmüller, A. Borbon, A. Schwarzenboeck, M. Merkel, M. Crippa, E. Kostenidou, M. Psichoudaki, L. Hildebrandt, G. J. Engelhart, T. Petäjä, A. S. H. Prévôt, F. Drewnick, U. Baltensperger,

- A. Wiedensohler, M. Kulmala, M. Beekmann, S. N. Pandis, In situ formation and spatial variability of particle number concentration in a European megacity. *Atmos. Chem. Phys.* **15**, 10219–10237 (2015). [doi:10.5194/acp-15-10219-2015](https://doi.org/10.5194/acp-15-10219-2015)
29. S. T. Martin, P. Artaxo, L. Machado, A. O. Manzi, R. A. F. Souza, C. Schumacher, J. Wang, T. Biscaro, J. Brito, A. Calheiros, K. Jardine, A. Medeiros, B. Portela, S. S. de Sá, K. Adachi, A. C. Aiken, R. Albrecht, L. Alexander, M. O. Andreae, H. M. J. Barbosa, P. Buseck, D. Chand, J. M. Comstock, D. A. Day, M. Dubey, J. Fan, J. Fast, G. Fisch, E. Fortner, S. Giangrande, M. Gilles, A. H. Goldstein, A. Guenther, J. Hubbe, M. Jensen, J. L. Jimenez, F. N. Keutsch, S. Kim, C. Kuang, A. Laskin, K. McKinney, F. Mei, M. Miller, R. Nascimento, T. Pauliquevis, M. Pekour, J. Peres, T. Petäjä, C. Pöhlker, U. Pöschl, L. Rizzo, B. Schmid, J. E. Shilling, M. A. S. Dias, J. N. Smith, J. M. Tomlinson, J. Tóta, M. Wendisch, The Green Ocean Amazon Experiment (GoAmazon2014/5) observes pollution affecting gases, aerosols, clouds, and rainfall over the rain forest. *Bull. Am. Meteorol. Soc.* **98**, 981–997 (2017). [doi:10.1175/BAMS-D-15-00221.1](https://doi.org/10.1175/BAMS-D-15-00221.1)
30. S. T. Martin, P. Artaxo, L. A. T. Machado, A. O. Manzi, R. A. F. Souza, C. Schumacher, J. Wang, M. O. Andreae, H. M. J. Barbosa, J. Fan, G. Fisch, A. H. Goldstein, A. Guenther, J. L. Jimenez, U. Pöschl, M. A. Silva Dias, J. N. Smith, M. Wendisch, Introduction: Observations and modeling of the Green Ocean Amazon (GoAmazon2014/5). *Atmos. Chem. Phys.* **16**, 4785–4797 (2016). [doi:10.5194/acp-16-4785-2016](https://doi.org/10.5194/acp-16-4785-2016)
31. S. E. Giangrande, S. Collis, J. Straka, A. Protat, C. Williams, S. Krueger, A summary of convective-core vertical velocity properties using ARM UHF wind profilers in Oklahoma. *J. Appl. Meteorol. Climatol.* **52**, 2278–2295 (2013). [doi:10.1175/JAMC-D-12-0185.1](https://doi.org/10.1175/JAMC-D-12-0185.1)
32. S. E. Giangrande, T. Toto, M. P. Jensen, M. J. Bartholomew, Z. Feng, A. Protat, C. R. Williams, C. Schumacher, L. Machado, Convective cloud vertical velocity and mass-flux characteristics from radar wind profiler observations during GoAmazon2014/5. *J. Geophys. Res. Atmos.* **121**, 12891–12913 (2016). [doi:10.1002/2016JD025303](https://doi.org/10.1002/2016JD025303)
33. S. Tang, S. Xie, Y. Zhang, M. Zhang, C. Schumacher, H. Upton, M. P. Jensen, K. L. Johnson, M. Wang, M. Ahlgrimm, Z. Feng, P. Minnis, M. Thieman, Large-scale vertical velocity, diabatic heating and drying profiles associated with seasonal and diurnal variations of convective systems observed in the GoAmazon2014/5 experiment. *Atmos. Chem. Phys.* **16**, 14249–14264 (2016). [doi:10.5194/acp-16-14249-2016](https://doi.org/10.5194/acp-16-14249-2016)
34. See supplementary materials.
35. J. A. Marengo, G. F. Fisch, L. M. Alves, N. V. Sousa, R. Fu, Y. Zhuang, Meteorological context of the onset and end of the rainy season in Central Amazonia during the 2014-15 Go-Amazon Experiment. *Atmos. Chem. Phys. Discuss.* 10.5194/acp-2017-22 (2017). [doi:10.5194/acp-2017-22](https://doi.org/10.5194/acp-2017-22)

36. A. P. Khain, A. Pokrovsky, M. Pinsky, A. Seifert, V. Phillips, Simulation of effects of atmospheric aerosols on deep turbulent convective clouds using a spectral microphysics mixed-phase cumulus cloud model. Part I: Model description and possible applications. *J. Atmos. Sci.* **61**, 2963–2982 (2004). [doi:10.1175/JAS-3350.1](https://doi.org/10.1175/JAS-3350.1)
37. J. Fan, L. R. Leung, Z. Li, H. Morrison, H. Chen, Y. Zhou, Y. Qian, Y. Wang, Aerosol impacts on clouds and precipitation in eastern China: Results from bin and bulk microphysics. *J. Geophys. Res.* **117**, D00K36 (2012). [doi:10.1029/2011JD016537](https://doi.org/10.1029/2011JD016537)
38. W. C. Skamarock *et al.*, *A Description of the Advanced Research WRF Version 3* (National Center for Atmospheric Research, 2008).
39. M. L. Pöhlker, F. Ditas, J. Saturno, T. Klimach, I. Hrabě de Angelis, A. Araùjo, J. Brito, S. Carbone, Y. Cheng, X. Chi, R. Ditz, S. S. Gunthe, K. Kandler, J. Kesselmeier, T. Könemann, J. V. Lavrič, S. T. Martin, E. Mikhailov, D. Moran-Zuloaga, L. V. Rizzo, D. Rose, H. Su, R. Thalman, D. Walter, J. Wang, S. Wolff, H. M. J. Barbosa, P. Artaxo, M. O. Andreae, U. Pöschl, C. Pöhlker, Long-term observations of cloud condensation nuclei in the Amazon rain forest – Part 2: Variability and characteristic differences under near-pristine, biomass burning, and long-range transport conditions. *Atmos. Chem. Phys. Discuss.* 10.5194/acp-2017-847 (2017). [doi:10.5194/acp-2017-847](https://doi.org/10.5194/acp-2017-847)
40. M. L. Pöhlker, C. Pöhlker, F. Ditas, T. Klimach, I. Hrabě de Angelis, A. Araùjo, J. Brito, S. Carbone, Y. Cheng, X. Chi, R. Ditz, S. S. Gunthe, J. Kesselmeier, T. Könemann, J. V. Lavrič, S. T. Martin, E. Mikhailov, D. Moran-Zuloaga, D. Rose, J. Saturno, H. Su, R. Thalman, D. Walter, J. Wang, S. Wolff, H. M. J. Barbosa, P. Artaxo, M. O. Andreae, U. Pöschl, Long-term observations of cloud condensation nuclei in the Amazon rain forest – Part 1: Aerosol size distribution, hygroscopicity, and new model parametrizations for CCN prediction. *Atmos. Chem. Phys.* **16**, 15709–15740 (2016). [doi:10.5194/acp-16-15709-2016](https://doi.org/10.5194/acp-16-15709-2016)
41. M. A. Cecchini, L. A. T. Machado, J. M. Comstock, F. Mei, J. Wang, J. Fan, J. M. Tomlinson, B. Schmid, R. Albrecht, S. T. Martin, P. Artaxo, Impacts of the Manaus pollution plume on the microphysical properties of Amazonian warm-phase clouds in the wet season. *Atmos. Chem. Phys.* **16**, 7029–7041 (2016). [doi:10.5194/acp-16-7029-2016](https://doi.org/10.5194/acp-16-7029-2016)
42. R. Zhang, G. Li, J. Fan, D. L. Wu, M. J. Molina, Intensification of Pacific storm track linked to Asian pollution. *Proc. Natl. Acad. Sci. U.S.A.* **104**, 5295–5299 (2007). [doi:10.1073/pnas.0700618104](https://doi.org/10.1073/pnas.0700618104) [Medline](#)
43. Y. Wang, M. Wang, R. Zhang, S. J. Ghan, Y. Lin, J. Hu, B. Pan, M. Levy, J. H. Jiang, M. J. Molina, Assessing the effects of anthropogenic aerosols on Pacific storm track using a multiscale global climate model. *Proc. Natl. Acad. Sci. U.S.A.* **111**, 6894–6899 (2014). [doi:10.1073/pnas.1403364111](https://doi.org/10.1073/pnas.1403364111) [Medline](#)



44. R. Zhang, A. Khalizov, L. Wang, M. Hu, W. Xu, Nucleation and growth of nanoparticles in the atmosphere. *Chem. Rev.* **112**, 1957–2011 (2012). [doi:10.1021/cr2001756](https://doi.org/10.1021/cr2001756) [Medline](#)
45. M. Shrivastava, C. D. Cappa, J. Fan, A. H. Goldstein, A. B. Guenther, J. L. Jimenez, C. Kuang, A. Laskin, S. T. Martin, N. L. Ng, T. Petaja, J. R. Pierce, P. J. Rasch, P. Roldin, J. H. Seinfeld, J. Shilling, J. N. Smith, J. A. Thornton, R. Volkamer, J. Wang, D. R. Worsnop, R. A. Zaveri, A. Zelenyuk, Q. Zhang, Recent advances in understanding secondary organic aerosol: Implications for global climate forcing. *Rev. Geophys.* **55**, 509–559 (2017). [doi:10.1002/2016RG000540](https://doi.org/10.1002/2016RG000540)
46. M. O. Andreae, A. Afchine, R. Albrecht, B. A. Holanda, P. Artaxo, H. M. J. Barbosa, S. Bormann, M. A. Cecchini, A. Costa, M. Dollner, D. Fütterer, E. Järvinen, T. Jurkat, T. Klimach, T. Konemann, C. Knote, M. Krämer, T. Krisna, L. A. T. Machado, S. Mertes, A. Minikin, C. Pöhlker, M. L. Pöhlker, U. Pöschl, D. Rosenfeld, D. Sauer, H. Schlager, M. Schnaiter, J. Schneider, C. Schulz, A. Spanu, V. B. Sperling, C. Voigt, A. Walser, J. Wang, B. Weinzierl, M. Wendisch, H. Ziereis, Aerosol characteristics and particle production in the upper troposphere over the Amazon Basin. *Atmos. Chem. Phys. Discuss.* 10.5194/acp-2017-694 (2017). [doi:10.5194/acp-2017-694](https://doi.org/10.5194/acp-2017-694)
47. J. Wang, M. Pikridas, S. R. Spielman, T. Pinterich, A fast integrated mobility spectrometer for rapid measurement of sub-micrometer aerosol size distribution, Part I: Design and model evaluation. *J. Aerosol Sci.* **108**, 44–55 (2017). [doi:10.1016/j.jaerosci.2017.02.012](https://doi.org/10.1016/j.jaerosci.2017.02.012)
48. J. A. Thornton, K. S. Virts, R. H. Holzworth, T. P. Mitchell, Lightning enhancement over major oceanic shipping lanes. *Geophys. Res. Lett.* **44**, 9102–9111 (2017). [doi:10.1002/2017GL074982](https://doi.org/10.1002/2017GL074982)
49. R. Gevaerd, S. R. Freitas, Estimativa operacional da umidade do solo para iniciação de modelos de previsão numérica da atmosfera. Parte I: descrição da metodologia e validação. *Rev. Bras. Meteorol.* **21**, 1–15 (2006).
50. V. Beck, C. Gerbig, T. Koch, M. M. Bela, K. M. Longo, S. R. Freitas, J. O. Kaplan, C. Prigent, P. Bergamaschi, M. Heimann, WRF-Chem simulations in the Amazon region during wet and dry season transitions: Evaluation of methane models and wetland inundation maps. *Atmos. Chem. Phys.* **13**, 7961–7982 (2013). [doi:10.5194/acp-13-7961-2013](https://doi.org/10.5194/acp-13-7961-2013)
51. H. Morrison, J. A. Curry, V. I. Khvorostyanov, A new double-moment microphysics parameterization for application in cloud and climate models. Part I: Description. *J. Atmos. Sci.* **62**, 1665–1677 (2005). [doi:10.1175/JAS3446.1](https://doi.org/10.1175/JAS3446.1)
52. H. Morrison, G. Thompson, V. Tatarskii, Impact of cloud microphysics on the development of trailing stratiform precipitation in a simulated squall line: Comparison of one- and two-moment schemes. *Mon. Weather Rev.* **137**, 991–1007 (2009). [doi:10.1175/2008MWR2556.1](https://doi.org/10.1175/2008MWR2556.1)



53. R. Thalman, S. S. de Sá, B. B. Palm, H. M. J. Barbosa, M. L. Pöhlker, M. L. Alexander, J. Brito, S. Carbone, P. Castillo, D. A. Day, C. Kuang, A. Manzi, N. L. Ng, A. J. Sedlacek III, R. Souza, S. Springston, T. Watson, C. Pöhlker, U. Pöschl, M. O. Andreae, P. Artaxo, J. L. Jimenez, S. T. Martin, J. Wang, CCN activity and organic hygroscopicity of aerosols downwind of an urban region in central Amazonia: Seasonal and diel variations and impact of anthropogenic emissions. *Atmos. Chem. Phys.* **17**, 11779–11801 (2017).  
[doi:10.5194/acp-17-11779-2017](https://doi.org/10.5194/acp-17-11779-2017)